OPEN ACCESS



The Epoch of Giant Planet Migration Planet Search Program. II. A Young Hot Jupiter Candidate around the AB Dor Member HS Psc*

Quang H. Tran¹, Brendan P. Bowler¹, William D. Cochran^{1,2}, Samuel Halverson³, Suvrath Mahadevan^{4,5,6}, Joe P. Ninan⁷, Paul Robertson⁸, Gudmundur Stefánsson^{9,11}, and Ryan C. Terrien¹⁰ Department of Astronomy, The University of Texas at Austin, 2515 Speedway, Stop C1400, Austin, TX 78712, USA; quangtran@utexas.edu

² McDonald Observatory and Center for Planetary Systems Habitability, USA

³ Jet Propulsion Laboratory, California Institute of Technology, 4800 Oak Grove Drive, Pasadena, CA 91109, USA

⁴ Department of Astronomy & Astrophysics, The Pennsylvania State University, 525 Davey Lab, University Park, PA 16802, USA

⁵ Center for Exoplanets & Habitable Worlds, University Park, PA 16802, USA

⁶ Penn State Astrobiology Research Center, University Park, PA 16802, USA

⁷ Department of Astronomy and Astrophysics, Tata Institute of Fundamental Research, Homi Bhabha Road, Colaba, Mumbai 400005, India

⁸ Department of Physics & Astronomy, The University of California, Irvine, Irvine, CA 92697, USA

⁹ Department of Astrophysical Sciences, Princeton University, 4 Ivy Lane, Princeton, NJ 08540, USA

¹⁰ Carleton College, One North College Street, Northfield, MN 55057, USA

Received 2023 August 15; revised 2024 February 20; accepted 2024 February 27; published 2024 April 4

Abstract

We report the discovery of a hot Jupiter candidate orbiting HS Psc, a K7 ($\approx 0.7~M_{\odot}$) member of the ≈ 130 Myr AB Doradus moving group. Using radial velocities over 4 yr from the Habitable-zone Planet Finder spectrograph at the Hobby–Eberly Telescope, we find a periodic signal of $P_b = 3.986^{+0.044}_{-0.003}$ days. A joint Keplerian and Gaussian process stellar activity model fit to the radial velocities yields a minimum mass of $m_p \sin i = 1.5^{+0.6}_{-0.4}~M_{\rm Jup}$. The stellar rotation period is well constrained by the Transiting Exoplanet Survey Satellite light curve ($P_{\rm rot} = 1.086 \pm 0.003~{\rm days}$) and is not an integer harmonic nor alias of the orbital period, supporting the planetary nature of the observed periodicity. HS Psc b joins a small population of young, close-in giant planet candidates with robust age and mass constraints and demonstrates that giant planets can either migrate to their close-in orbital separations by 130 Myr or form in situ. Given its membership in a young moving group, HS Psc represents an excellent target for follow-up observations to characterize this young hot Jupiter further, refine its orbital properties, and search for additional planets in the system.

Unified Astronomy Thesaurus concepts: Exoplanet astronomy (486); Exoplanet evolution (491); Radial velocity (1332)

Supporting material: machine-readable table

1. Introduction

The processes by which the closest-in ($P_{\rm orb}\lesssim 10$ days) giant planets arrive at their present-day locations remain challenging to constrain observationally. Several formation and migration mechanisms have been introduced to account for this population of hot Jupiters (HJs; Dawson & Johnson 2018). These include in situ formation (e.g., Batygin et al. 2016; Boley et al. 2016), disk migration (e.g., Goldreich & Tremaine 1980; Ward 1997; Kley & Nelson 2012), or more "violent" scenarios of three-body dynamical interactions such as planet–planet scattering or von Zeipel–Lidov–Kozai interactions coupled with high-eccentricity tidal migration (e.g., Wu & Murray 2003; Fabrycky & Tremaine 2007; Triaud et al. 2010; Naoz et al. 2011). However, as the timescales of these processes (≈ 1 Myr–1 Gyr) are shorter than the typical ages of

¹¹ NASA Sagan Fellow.

Original content from this work may be used under the terms of the Creative Commons Attribution 4.0 licence. Any further distribution of this work must maintain attribution to the author(s) and the title of the work, journal citation and DOI.

observed systems, our knowledge of HJ evolutionary pathways is limited.

Young giant planets are valuable because they provide a means to distinguish among these mechanisms, which operate on different characteristic timescales. However, the detection and characterization of young HJs has been hindered by the presence of stellar activity, making these systems challenging to find and validate. As a result, many proposed young HJs have been disputed, rejected, or lack independent confirmation (e.g., Figueira et al. 2010; Hernán-Obispo et al. 2010; van Eyken et al. 2012; Hernán-Obispo et al. 2015; Carleo et al. 2018; Tuomi et al. 2018; Bouma et al. 2020b; Carleo et al. 2020; Carmona et al. 2023). Notable examples of young HJs include V830 Tau b, TAP 26 b, and CI Tau b (Donati et al. 2016; Johns-Krull et al. 2016; Yu et al. 2017).

More recently, a growing number of large transiting planets has been found orbiting young stars, such as K2-33 b (David et al. 2016; Mann et al. 2016), HIP 67522 b (Rizzuto et al. 2020), and TOI-837 b (Bouma et al. 2020a), with radii consistent with Jupiter-sized planets ($R_p \ge 0.5 R_{\rm Jup}$). However, these systems lack precise mass measurements. As such, it is difficult to determine whether these systems are truly young HJs or instead are inflated Neptunes that have yet to shrink, either from gravitational contraction as they cool or through atmospheric mass loss (e.g., Fortney et al. 2007; Lopez et al. 2012; Owen & Wu 2013; Gupta & Schlichting 2019, 2020), as

^{*} Based on observations obtained with the Hobby–Eberly Telescope (HET), which is a joint project of the University of Texas at Austin, the Pennsylvania State University, Ludwig-Maximillians-Universitaet Muenchen, and Georg-August Universitaet Goettingen. The HET is named in honor of its principal benefactors, William P. Hobby and Robert E. Eberly.

Table 1
Properties of HS Psc

Property	Value	References
Gaia DR3 ID	295713106830535424	(1)
TIC ID	353804063	(2)
Two Micron All Sky Survey (2MASS) ID	J01372322+2657119	(3)
$\alpha_{2000.0}$	01:37:23.38	(1)
$\delta_{2000.0}$	+26:57:10.03	(1)
$_{\alpha}^{a}$ (mas yr ⁻¹)	118.237 ± 0.022	(1)
μ_{δ} (mas yr ⁻¹)	-127.589 ± 0.020	(1)
(mas)	26.486 ± 0.018	(1)
Distance (pc)	$37.667^{+0.038}_{-0.044}$	(1)
RUWE _{DR3}	1.055	(1)
(mag)	10.292 ± 0.004	(1)
G_{RP} (mag)	9.455 ± 0.007	(1)
G_{BP} (mag)	11.024 ± 0.009	(1)
B (mag)	12.027 ± 0.053	(4)
V (mag)	10.855 ± 0.063	(4)
J (mag)	8.429 ± 0.023	(3)
H (mag)	7.784 ± 0.021	(3)
K_s (mag)	7.642 ± 0.027	(3)
W ₁ (mag)	7.515 ± 0.031	(5)
W ₂ (mag)	7.557 ± 0.021	(5)
SpT	K7V	(6)
Mass (M_{\odot})	0.69 ± 0.07	(7)
Radius (R_{\odot})	0.65 ± 0.07	(7)
Luminosity (L_{\odot})	0.122 ± 0.007	(7)
$T_{\rm eff}$ (K)	4203 ± 116	(7)
$\log g (\text{dex})^{\text{b}}$	4.66 ± 0.03	(7)
[Fe/H] (dex)	-0.05 ± 0.09	(7)
$v \sin i_* \text{ (km s}^{-1}\text{)}$	29.7 ± 3.1	(7)
$v_{\rm eq} ({\rm km \ s^{-1}})$	29.7 ± 2.8	(7)
<i>i</i> * (°)	90^{+0}_{-22}	(7)
$P_{\rm rot}$ (day)	1.086 ± 0.003	(7)
Age (Myr)	133^{+15}_{-20}	(8)

Notes.

References. (1) Gaia Collaboration et al. (2022); (2) Stassun et al. (2019); (3) Cutri et al. (2003); (4) Zacharias et al. (2012); (5) Cutri et al. (2021); (6) Bowler et al. (2019); (7) this work; and (8) Gagné et al. (2018a).

has been suggested for systems discovered in young clusters (e.g., Mann et al. 2017; Rizzuto et al. 2018).

Given these challenges and the intrinsically low occurrence rate of HJs at field ages ($1.2\% \pm 0.38\%$; Wright et al. 2012), each young system provides valuable information about the origin and dynamical evolution of this class of giant planets. Building a statistically robust sample of young HJs provides clues about the migration history and physical mechanism producing close-in giant planets.

The Epoch of Giant Planet Migration planet search program is an ongoing long-baseline, near-infrared (NIR) precision radial velocity (RV) survey targeting young, nearby Sun-like stars (Tran et al. 2021). Our targets comprise bona fide and high-probability candidate members of 10 young moving groups—AB Dor, β Pic, Carina, Carina-Near, Octans, Tuc-Hor, Pleiades, 32 Ori, Argus, and Pisces—with ages between 20 and 200 Myr. Known binaries and fast rotators (ν sin $i_* > 35$ km s⁻¹) are removed to produce a sample consistent with giant planet RV search programs of older field stars (e.g., Johnson et al. 2010). By observing in the NIR, as

opposed to the optical, our program leverages the wavelength dependence of spot-driven activity signals to minimize RV contributions from astrophysical jitter. This opens the possibility of detecting massive, close-in young planets with RV semiamplitudes comparable to the reduced activity signals. The goal of this survey is to measure the occurrence rate of close-in giant planets at young ages, compare this frequency with similar measurements at older ages, and constrain the dominant timescale and mechanism of giant planet migration.

Here, we present the discovery of a HJ candidate orbiting the young star HS Psc with the Habitable-zone Planet Finder (HPF) spectrograph at McDonald Observatory's Hobby–Eberly Telescope (HET). In Section 2, we summarize the physical parameters and previous observations of HS Psc. We describe the Transiting Exoplanet Survey Satellite (TESS) photometry and the HPF RV observations of HS Psc in Section 3. Characterization of the system, including the host star and modeling of the HPF RVs, is presented in Section 4. In Section 5, we discuss the implications of this discovery and follow-up observations that would be helpful to validate and characterize HS Psc b further. Finally, we summarize our results in Section 6.

2. HS Psc: A Young Sun-like Star

HS Psc is a bright (V=10.86 mag; Zacharias et al. 2013) K7V star (Bowler et al. 2019) in the AB Dor moving group (Schlieder et al. 2010; Malo et al. 2013; Gagné et al. 2018b). It has an age of 133^{+15}_{-20} Myr from its cluster membership (Gagné et al. 2018a), a parallactic distance of $37.667^{+0.038}_{-0.044}$ pc (Gaia Collaboration et al. 2022), and a stellar isochrone-inferred mass of $0.69\pm0.07~M_{\odot}$ (Section 4.2). Table 1 summarizes the kinematic, photometric, and physical properties of HS Psc.

As a young, bright, nearby star, HS Psc has been observed several times by direct-imaging exoplanet search programs. Brandt et al. (2014) targeted HS Psc with with HiCIAO differential imaging instrument (Suzuki et al. 2010) at the Subaru Telescope as part of the Strategic Exploration of Exoplanets and Disks with Subaru program. They detected a faint point source at a projected distance of approximately 200 au (\approx 5."3) but did not recover it in follow-up observations. Bowler et al. (2015) also acquired deep observations of HS Psc with Keck/NIRC2 in K_s band, reaching contrasts of $\Delta K_s = 9.0$ mag at 0."5 and $\Delta K_s = 11.6$ mag at 1". Bowler et al. (2019) obtained shallow optical high-resolution imaging of HS Psc with Robo-AO at the Palomar 1.5 m telescope. No nearby substellar or stellar companions were present within the detection limits of both data sets.

Gaia DR3 reports a renormalized unit weight error (RUWE) of 1.055 for HS Psc (Gaia Collaboration et al. 2021, 2022). RUWE values greater than 1.4 indicate that the single-star model is a poor fit to the astrometric solution (Lindegren 2018; Stassun & Torres 2021), so the RUWE value for HS Psc does not indicate the presence of a binary companion. Furthermore, the rms of our precise RVs over 4 yr in Section 3.2 implies that we can rule out a close-in massive companion for most orbital orientations. Altogether HS Psc appears to be a single young star with no nearby binary companions in the stellar or brown dwarf (BD) regimes, within the detection limits of current imaging and RV surveys.

^a Proper motion in R.A. includes a factor of $\cos \delta$.

b In cgs units

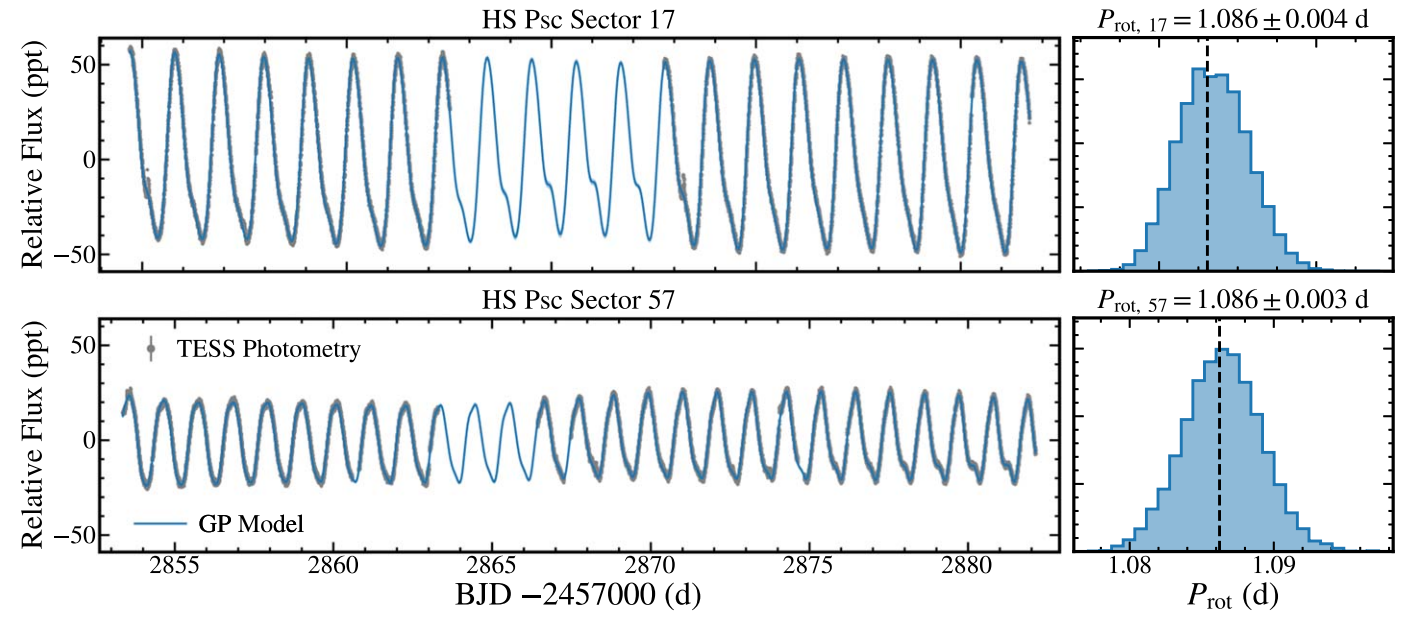


Figure 1. TESS Sector 17 (top) and 57 (bottom) light curves of HS Psc. The best-fit mean GP model and 1σ variance are displayed as solid blue lines and shaded regions, respectively. The posterior distributions and MAP values (dashed vertical line) for the QP GP P_{rot} hyperparameter for TESS Sectors 17 and 57 are shown in the right panels. The GP model separately recovers rotation periods of $P_{\text{rot},17} = 1.086 \pm 0.003$ days and $P_{\text{rot},57} = 1.086 \pm 0.004$ days for Sectors 17 and 57, respectively.

3. Observations

3.1. TESS Photometry

The Transiting Exoplanet Survey Satellite (TESS; Ricker et al. 2015) observed HS Psc at 2 minute cadence in Sectors 17 (UT 2019 October 8 to 2019 November 2) and 57 (UT 2022 September 30 to 2022 October 29). The light curves were retrieved and processed following the procedure described in Bowler et al. (2023). We downloaded the Science Processing Operations Center (Jenkins et al. 2016) Pre-search Data Conditioning Simple Aperture Photometry (PDCSAP) light curve (Smith et al. 2012; Stumpe et al. 2012, 2014) from the MAST data archive¹² using the lightkurve (Lightkurve Collaboration et al. 2018) software package. All photometric measurements flagged as poor (DQUALITY > 0) or are listed as NaN are removed. Each TESS sector is first median normalized and then stitched together. Outlier points from flares and artifacts are removed by flattening the light curve using a highpass Savitzky-Golay filter (Savitzky & Golay 1964) and excluding all data outside of three standard deviations of the flattened light curve. The TESS light curves for Sectors 17 and 57 are displayed in the left panels of Figure 1.

3.2. HPF Spectroscopy

As part of our initial results from the Epoch of Giant Planet Migration program, Tran et al. (2021) measured an RV rms of over 200 m s⁻¹ for HS Psc with eight RV epochs. This system was an outlier among our sample of young stars, which had a median RV rms of only 34.3 m s⁻¹. As this anomalously high RV scatter could potentially be explained by a close-in giant planet, we increased our monitoring cadence of this system over the following 3 yr.

We used HPF on the HET (Ramsey et al. 1998; Hill et al. 2021) to obtain a total of 83 spectra of HS Psc between UT 2018 November and UT 2022 November. HPF is a NIR (0.81–1.27 μ m), fiber-fed (Kanodia et al. 2018), environment-stabilized (Mahadevan et al. 2012, 2014; Stefansson et al. 2016) high-resolution échelle spectrograph. Wavelength calibration is achieved with a laser frequency comb (Metcalf et al. 2019). HPF has 28 spectral orders with an average resolving power of $R \equiv \lambda/\Delta\lambda = 55,000$ (Mahadevan et al. 2012; Ninan et al. 2019).

Observations are obtained and RVs are measured following the procedures detailed in Tran et al. (2021). HET's flexible scheduling system allows observations to be taken in queue mode (Shetrone et al. 2007). During each epoch, three contiguous exposures are obtained to sample high-frequency variations. All exposures have a 300 s integration time and the average signal-to-noise ratio (S/N) at 1.07 μ m is 115 ± 30 pixel⁻¹. 1D spectra are optimally extracted using the custom HPF data-reduction pipeline following the procedures described in Ninan et al. (2018), Kaplan et al. (2019), and Metcalf et al. (2019).

Relative RVs, differential line widths (dLWs), and chromatic indices (CRXs) are measured using a custom least-squares matching pipeline based on the SpEctrum Radial Velocity AnaLyser (SERVAL) code (Zechmeister et al. 2018; Tran et al. 2021). Furthermore, the line indices of the Ca II infrared triplet (Ca II IRT) emission lines are measured following Stefansson et al. (2020b). We use the eight échelle orders corresponding to wavelength ranges in the z band (8535–8895 Å) and Y band (9933–10767 Å) for the RV extraction to avoid contamination of strong telluric absorption (orders 4, 5, 6, 14, 15, 16, 17, and 18; Tran et al. 2021). The RV and activity indicator measurements are reported in Table A1 in Appendix A.

From UT 2022 May to June, HPF underwent a vacuum warm-up and cool-down cycle so maintenance work could be carried out on the detector. This has introduced a velocity offset in the RV time series. To account for this unknown offset, RVs obtained prior to and after this downtime are treated as if they

¹² https://archive.stsci.edu/missions-and-data/tess. All TESS data used are available at MAST: doi:10.17909/t9-nmc8-f686 (MAST Team 2021).

are measurements from two different instruments when searching for planets and modeling Keplerian signals. In this work, we label the RV measurements prior to this maintenance "prewarmup" HPF1 and measurements after "postwarmup" HPF2 to distinguish between the two observing periods. Altogether there are $N_{\rm RV,\,HPF1}=62$ and $N_{\rm RV,\,HPF2}=21$ observations associated with HPF1 and HPF2, respectively. The prewarmup RVs have an rms of RV_{rms, HPF1} = 262 m s⁻¹ and an average RV measurement uncertainty of $\bar{\sigma}_{\rm RV,\,HPF1}=124\,{\rm m\,s^{-1}}$. The postwarmup RVs have an rms of RV_{rms, HPF2} = 264 m s⁻¹ and an average RV measurement uncertainty of $\bar{\sigma}_{\rm RV,\,HPF2}=150\,{\rm m\,s^{-1}}$. These large measurement uncertainties are primarily driven by the large rotational velocity (see Section 4.1) of HS Psc.

4. Results

4.1. Spectroscopic Parameters

We determine the spectroscopic properties of HS Psc following the empirical spectral matching procedure as described in Stefansson et al. (2020a), which is based on the SpecMatch-Emp algorithm of Yee et al. (2017). This technique compares a science spectrum with a library of high-S/N spectra of slowly rotating stars and identifies the best match between the stellar and library spectra. During each fit, the reference star spectrum is convolved with a broadening kernel (Gray 1992) in order to estimate the rotational velocity. The final values are estimated from a composite spectrum of the five best-fitting reference spectra.

Using the highest-S/N HPF (S/N = 150) spectrum as the science target, we measure the effective temperature $(T_{\rm eff})$, metallicity ([Fe/H]), surface gravity ($\log g$), and projected rotational velocity ($v \sin i_*$) of HS Psc. The procedure is applied to the same eight HPF échelle orders used for RV extraction. Uncertainties on T_{eff} , [Fe/H], and $\log g$ are calculated for each échelle order using a cross-validation method following Stefansson et al. (2020a), which iteratively removes each library spectrum from the sample, fits for $T_{\rm eff}$, [Fe/H], and log g using the interpolated grid, and compares the best-fit measurement to the known library value. The standard deviation of the residuals between the recovered and library values is adopted as the uncertainty of each parameter for each échelle order. The weighted mean and weighted standard deviation of the spectral order measurements are used as the final values and uncertainties for each parameter. This crossvalidation method cannot determine uncertainties on $v \sin i_*$ as all library spectra are of slowly rotating stars. Thus, for $v \sin i_*$, we adopt the median value and standard deviation of the eight échelle order values. We find an effective temperature of $T_{\rm eff} = 4203 \pm 116$ K, a metallicity of [Fe/H] = -0.05 ± 0.09 dex, a surface gravity of $\log g = 4.66 \pm 0.03$ dex, and a stellar rotational velocity of $v \sin i_* = 29.7 \pm 3.1 \,\mathrm{km \, s}^{-1}$ for HS Psc.

These values are consistent with measurements reported in the literature. McCarthy & White (2012) found $T_{\rm eff}=4400\pm105~{\rm K}$ using low-resolution ($R\sim3575$) optical spectra. Stassun et al. (2019) report an effective temperature of $T_{\rm eff}=4215\pm128~{\rm K}$ and a surface gravity of $\log g=4.64\pm0.11~{\rm dex}$. Barenfeld et al. (2013) found a near-solar representative metallicity for the AB Dor moving group of [Fe/H] = $0.02\pm0.02~{\rm dex}$.

Schlieder et al. (2010) report a much lower rotational velocity of $v \sin i_* = 10 \pm 2 \,\mathrm{km \, s^{-1}}$ using spectra from CSHELL (Greene et al. 1993). This discrepancy between

 $v \sin i_*$ measured using our HPF and their CSHELL spectra may be due to the lower resolution of CSHELL, which can be as low as R = 5000, depending on the slit choice. In Tran et al. (2021), we previously measured a relatively uncertain projected rotational velocity of $v \sin i_* = 22 \pm 8 \text{ km s}^{-1}$. Our new measurement of $v \sin i_* = 29.7 \pm 3.1 \text{ km s}^{-1}$ is more precise and based on empirical templates instead of synthetic models.

4.2. Stellar Mass and Radius

For T_{eff} , $\log g$, and [Fe/H], we adopt Gaussian priors with means and standard deviations set to the values and uncertainties reported in Section 4.1. The distance prior uses a Gaussian distribution with the mean and standard deviation set to the Gaia DR3 distance estimate and the larger of the upper and lower uncertainties, $\mathcal{N}(37.667, 0.044)^{13}$ pc, the stellar radius prior set to a Gaussian distribution with the mean and standard deviation set to the Gaia DR3 Final Luminosity Age Mass Estimator (Gaia Collaboration et al. 2018) derived radius and uncertainty, $\mathcal{P}(R_*) = \mathcal{N}(0.6561, 0.019) R_{\odot}$, and the line-of-sight extinction prior set to a uniform distribution with an upper limit set to the maximum line-of-sight ($A_{V,\text{max}} = 0.235 \text{ mag}$) extinction from the SFD Galactic dust map (Schlegel et al. 1998; Schlafly & Finkbeiner 2011) as determined by the software package dustmaps (Green 2018). The excess photometric noise terms all have Gaussian priors centered at zero with a standard deviation equal to 10 times the photometric uncertainty of each band.

The posterior distributions of all fitted parameters in the model are sampled using the dynamic nested sampler dynesty (Skilling 2004, 2006; Speagle 2020; Koposov et al. 2023). The sampling is initialized with 5000 live points and terminates when the evidence tolerance reaches a threshold of dlogz < 0.1. From this fit to the SED, we infer a stellar radius of $R_* = 0.65 \pm 0.01~R_{\odot}$. The parameters derived from the grid interpolation are $T_{\rm eff} = 4232^{+45}_{-38}~{\rm K}$, $\log g = 4.66 \pm 0.03~{\rm dex}$, and $[{\rm Fe/H}] = -0.08^{+0.08}_{-0.07}~{\rm dex}$, which are consistent with the values measured in Section 4.1. The bolometric luminosity computed from the SED-fitting procedure is $L_* = 0.121 \pm 0.006~L_{\odot}$. Using the derived radius and surface gravity, we estimate a mass of $M_* = 0.70 \pm 0.05~M_{\odot}$ for HS Psc. However, this mass is sensitive to the inferred surface gravity.

We also infer the mass of HS Psc using the open software package isochrones (Morton 2015). isochrones determines fundamental stellar properties by fitting combinations of photometric bandpasses and physical values to synthetic values

 $[\]overline{^{13}}$ $\mathcal{N}(a, b)$ refers to the normal distribution with a mean of a and standard deviation of b.

generated using interpolated grids of evolutionary models. For the fitting routine, we utilize the MESA Isochrones and Stellar Tracks (Choi et al. 2016; Dotter 2016) evolutionary model grids, all broadband photometry listed in Table 1, all parameters measured in Section 4.1, and the Gaia DR3 parallax.

As isochrones samples the age parameter as $\log_{10}(age)$, we set a flat prior in log space based on the AB Dor moving group age, $\mathcal{P}(\tau_*) = \log \mathcal{U}[113, 148]^{14}$ Myr. We also adopt a Gaussian prior based on the representative metallicity of the AB Dor moving group from Barenfeld et al. (2013), $\mathcal{P}([\text{Fe/H}]) = \mathcal{N}(0.02, 0.02)$ dex. For the distance and extinction priors, we adopt the same priors as in the SED fitting, $\mathcal{P}(\text{distance}) = \mathcal{N}(37.667, 0.044)$ pc and $\mathcal{P}(A_V) = \mathcal{U}[0, 0.235]$ mag, respectively. Following the default distribution adopted by isochrones, the mass prior follows the lognormal initial mass function from Chabrier (2003, Equation (17)).

The posterior distributions of all fit and derived parameters are sampled with the multimodal nested sampling algorithm MultiNest (Feroz et al. 2009, 2019) using the open software package PyMultiNest (Buchner et al. 2014). We initialize the sampling with 5000 live points. The best-fit stellar mass and radius are $M_*=0.686\pm0.003~M_{\odot}$ and $R_*=0.628\pm0.002~R_{\odot}$, respectively. The best-fit inferred parameters are $T_{\rm eff}=4338\pm9~{\rm K}$, $\log g=4.679\pm0.001~{\rm dex}$, and $\rm [Fe/H]=0.10\pm0.02~{\rm dex}$, which are consistent with the measurements adopted in Section 4.1 to within 2σ . Altering the age, metallicity, and distance priors do not substantially change these results.

As a comparison to these measurements, we also report masses and radii estimated using relationships with other parameters such as the effective temperature, metallicity, and luminosity. Combining the parameters derived in Section 4.1 with the empirical functions calibrated using 190 stars from Torres et al. (2010) relating $T_{\rm eff}$, $\log g$, and [Fe/H] to M_* and R_* yields a stellar mass and radius of $M_*=0.60\pm0.04~M_\odot$ and $R_*=0.59\pm0.02~R_\odot$, respectively. Similarly, using the Stefan–Boltzmann law, the SED-computed luminosity ($L_*=0.121\pm0.006~L_\odot$), and our adopted effective temperature ($T_{\rm eff}=4203\pm116~{\rm K}$) returns a radius of $R_*=0.66\pm0.04~R_\odot$. Stassun et al. (2019) estimates a mass and radius of $M_*=0.66\pm0.08~M_\odot$ and $R_*=0.647\pm0.062~R_\odot$, respectively, for HS Psc.

We adopt the stellar radius and mass inferred with ARIADNE and isochrones, respectively. Given the range of inferred masses and radii in our analysis and compared with similar dispersion in estimates for other K7V members of the AB Dor moving group, we conservatively adopt a flat 10% estimate for the uncertainty in both parameters. This is larger than the characteristic scatter of inferred masses and radii for comparatively old main-sequence stars (\sim 5%; Tayar et al. 2022). The final adopted stellar mass and radius for HS Psc is $M_* = 0.69 \pm 0.07~M_{\odot}$ and $R_* = 0.65 \pm 0.07~R_{\odot}$, respectively.

4.3. Rotation Period, Stellar Inclination, and Transit Search

The TESS light curve of HS Psc exhibits clear and consistent modulation at the levels of 5% and 2.5% during Sectors 17 and 57, respectively. While the amplitude (and to a lesser degree the phase) of the signal changes between the two observational windows, its periodicity does not. This suggests that the

observed variability is driven by long-lived spots on the stellar surface and therefore can be used to estimate the stellar rotation period accurately.

The rotation period is derived by independently fitting a quasiperiodic (QP) Gaussian process (GP) to each TESS Sector light curve. QP GPs have been shown to infer stellar rotation periods from photometric time series accurately (e.g., Angus et al. 2018). The TESS sectors are treated separately as significant evolution has occurred in the 2.91 yr between Sectors 17 and 57 (Figure 1). We bin the TESS photometry to 30 minute cadence to improve computational efficiency while retaining large-scale, activity-driven structure. We use a QP kernel of the form:

$$k_{\rm QP}(\tau) = A^2 \exp\left(-\frac{\tau^2}{2l^2} - \frac{2\sin^2\left(\frac{\pi\tau}{P_{\rm rot}}\right)}{\theta^2}\right),\tag{1}$$

where τ is the time interval between any two points in time t_i and t_j , $|t_i - t_j|$, A is the amplitude, l is the local correlation timescale, P_{rot} is the stellar rotation period, and θ is the smoothness of the periodic correlation.

We use the emcee open Python package (Foreman-Mackey et al. 2013, 2019) to sample the posteriors of the kernel hyperparameters and an additional white-noise jitter term, $\sigma_{\rm iit}$. We impose noninformative uniform priors for each hyperparameter: for A, l, θ , σ_{jit} , and P_{rot} , we adopt $\mathcal{P}(A) =$ $\mathcal{U}[0.01, 5000] \text{ ppt}, \mathcal{P}(l) = \mathcal{U}[0.001, 10], \mathcal{P}(\theta) = \mathcal{U}[0.001, 10],$ $\mathcal{P}(\sigma_{\text{iit}}) = \mathcal{U}[\log(0.001), \log(100)]$ ppt, and $\mathcal{P}(P_{\text{rot}}) = \mathcal{U}[0.1,$ 10] days, respectively. Sampling is initialized with 50 walkers and 10,000 steps, for a total of 5×10^6 samples, where the first 50% are removed as burn-in and convergence is confirmed using the autocorrelation time. We adopt the $P_{\rm rot}$ maximum a posterori (MAP) value and standard deviation of the posteriors as the rotation period measurement and uncertainty. We find separate rotation periods of $P_{\text{rot},17} = 1.086 \pm 0.003$ days and $P_{\text{rot},57} = 1.086 \pm 0.004$ days for TESS Sectors 17 and 57, respectively.

These rotation periods are consistent with the values derived from the SuperWASP ($P_{\rm rot}=1.0852$ days; Norton et al. 2007) and KELT ($P_{\rm rot}=1.0859$ days; Oelkers et al. 2018) photometric surveys. Thus, we safely adopt the weighted mean and mean error of the two TESS Sectors, $P_{\rm rot}=1.086\pm0.003$ days, as the stellar rotation period of HS Psc. The processed TESS light curves and marginalized $P_{\rm rot}$ posteriors for Sectors 17 and 57 are displayed in Figure 1.

Using the rotation period, stellar radius, and projected rotational velocity, we infer the line-of-sight stellar inclination, i_* , following the Bayesian framework from Masuda & Winn (2020). We utilize the analytical expressions described in Bowler et al. (2023, Equation (9)) to obtain the posterior distribution of i_* while accounting for the correlation between the projected and equatorial rotational velocities. Here, we adopt the TESS rotation period of $P_{\rm rot} = 1.086 \pm 0.003$ days, a stellar radius of $R_* = 0.65 \pm 0.07$ R_{\odot} , and a projected rotational velocity of $v \sin i_* = 29.7 \pm 3.1$ km s⁻¹. It is evident, given the projected rotational velocity, $v \sin i_* = 29.7 \pm 3.1$ km s⁻¹, and the equatorial velocity, $2\pi R_*/P_{\rm rot} = v_{\rm eq} = 29.7 \pm 2.8$ km s⁻¹, that HS Psc is seen approximately equator on. We find a MAP value of 83°, a 68% credible interval spanning 67°–90°, and a 95% credible interval spanning 52°–90° for the stellar inclination.

 $^{^{14}}$ $\mathcal{U}[a,b]$ refers to a uniform distribution bounded by and inclusive of lower limit a and upper limit b.

As a close-in giant planet, HS Psc b's geometric transit probability is relatively high at \approx 6%. We use the Notch filter and Locally Optimized Combination of Rotations (LOCoR) detrending algorithms (Rizzuto et al. 2017) to search for potential transit events in the TESS light curve. The Notch and LOCoR filters use a combination of a transit-shaped notch and quadratic continuum to search for transit-like events in small windows of the light curve. These algorithms have been used to discover planets smaller than Jupiter transiting young ($\tau_* < 100$ Myr) stars (e.g., Rizzuto et al. 2018; Newton et al. 2019; Rizzuto et al. 2020).

We run the Notch filter to detrend the original TESS light curve 15 and, as HS Psc is a fast rotator, we apply the LOCoR algorithm to account for aliases of its rotation period $(P_{\rm rot}=1.086\pm0.003~{\rm days})$. Using various window sizes $(0.05-0.5~{\rm days})$, we do not detect a signal at the periodicity of the planet $(P_b=3.986~{\rm days})$ in the detrended light curves. Several strong signals do emerge at other periodicities, but inspection of the phase-folded, detrended light curves at those observed periods and times of inferior conjunction indicate that these signals are artifacts of the detrending process or remnants of stellar activity that were not detrended.

4.4. Periodogram and Stellar Activity Analysis

To search for periodic signals from planets and investigate the stellar activity of HS Psc, we compute the generalized Lomb–Scargle (GLS) periodogram of the RV observations and associated activity indicators over the frequency range 0.0005–1.0526 day⁻¹ (0.95–2000 days). This upper frequency limit near 1 day corresponds to the first peak of the spectral window function (WF), which is caused by a strong sampling alias resulting from nightly observations frequently seen in ground-based observations. This frequency represents the lowest limit at which the data can reliably identify periodicities. The periodograms are calculated on the concatenated sets of measurements (HPF₁ and HPF₂).

To test if the choice to combine HPF₁ and HPF₂ measurements impacts our results, we calculate the GLS periodogram with both the LombScargle and the LombScargleMultiband classes in the open-source Python package astropy.timeseries (Astropy Collaboration et al. 2013, 2018, 2022), which are designed to treat single time series and multiband time series, respectively. We also calculate GLS periodograms for the concatenated RVs after subtracting the average of each data set and after subtracting the derived RV offsets. Furthermore, we also calculate periodograms for the RV data separated by even and odd observations and in two halves. We find that all periodograms are similar to each other and the periodogram features remain robust against these changes. We thus safely choose to calculate the single-band periodogram for the concatenated measurements for further analysis.

Figure 2 displays the GLS periodograms for the RV observations, the associated activity indicators (dLWs, CRXs, and line indices of the Ca II IRT), the RV residuals after subtracting the best-fit planetary model (Section 4.5), and the spectral WF over the period range of 0.95–50 days. The false alarm probabilities (FAPs) at the 1% and 0.01% levels are

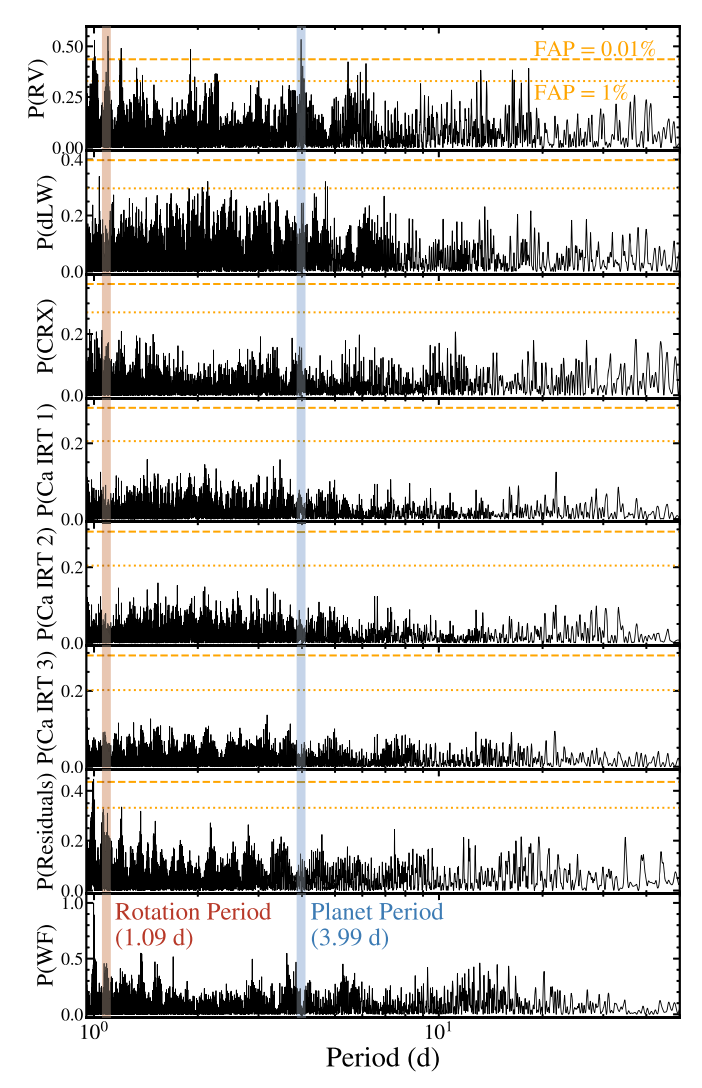


Figure 2. GLS periodograms of the spectral time series. Beginning with the top panel, the periodograms are calculated for the HPF RVs, the dLW activity indicator, the CRX, the Ca II IRT indices for the Ca II 1, 2, and 3 IRT emission lines, the RV residuals after subtracting the best-fit planetary model, and the spectral WF. The planet orbital period ($P_b = 3.99$ days) and the stellar rotation period ($P_{\rm rot} = 1.086$ days) are highlighted in the blue and red vertical shaded regions, respectively. FAPs of 1% and 0.01%, calculated using the bootstrap method, are shown as orange dotted and dashed lines, respectively. There are five peaks above the FAP = 0.01% threshold in the periodogram of the RVs; these represent the nightly sampling alias (seen at 1.0 day in the bottom panel with the WF periodogram), the stellar rotation period, the orbital period, and likely aliases of the stellar rotation and orbital periods.

calculated using the bootstrap method and are shown in dotted and dashed orange lines, respectively.

Five peaks rise above the 0.01% threshold in the RV periodogram. A peak at 1.003 days corresponds to an alias caused by nightly sampling, which is also seen in the WF periodogram. Significant peaks appear near the rotation period (1.09 days) and a likely alias sequence of the rotation period (~ 1.2 days). Finally, two significant peaks are observed at 3.99 days and a possible harmonic alias of this signal, 1.91 days. We interpret the ≈ 4 day signal as a planet candidate, as no significant peaks emerge in the activity indicators at or near this frequency. No additional periodic signals that may have been overwhelmed by the initial planetary signal emerge in the periodogram of the residuals; only the ~ 1 day synoptic nightly sampling alias remains significant at the FAP = 0.01% level.

 $[\]overline{^{15}}$ Transit searches are conducted on the PDCSAP light curve prior to normalization and sigma-clipping as described in Section 3.1.

To test further for correlations between the RVs and associated spectral indicators, we compute the Pearson's correlation coefficient (Pearson's r) and p-values between the RVs and activity indicators (see Section 3.2). This test is conducted as spectral indicators that trace distortions in the spectral line profile induced by starspots may correlate with RV measurements (e.g., Queloz et al. 2001; Boisse et al. 2011; Meunier & Lagrange 2013). Here, r-values measure correlation strength, ranging from -1 for a perfect anticorrelation and 1 for a perfect correlation. p-values report the probability of observing a corresponding r-value if the data are not correlated, so a lower p-value represents a higher probability that the data are correlated. For the HPF RVs and associated activity indicators, all Pearson's r-values have an absolute value less than 0.5 and all p-values are greater than 0.05, indicating that none of the activity indicators are significantly correlated with the HPF RVs. The maximum correlation coefficient is r = 0.4, with a p-value of 0.07, for the HPF₂ RVs and the corresponding Ca II IRT 2 line index. The other Ca II IRT indices have similar *r*-values.

4.5. Radial Velocities and Gaussian Process Modeling

The youth and persistent photometric variability of HS Psc signifies that strong, correlated, starspot-driven modulations should be present in the RV observations of HS Psc b. Rednoise GP models are now commonly employed to fit RV variability arising from stellar activity (e.g., Affer et al. 2016; Damasso & Del Sordo 2017; Faria et al. 2020; Stefansson et al. 2022). To take into account the expected correlation of RV signals caused by stellar activity, we perform three separate model fits to the HPF RVs that vary in their treatment of stellar activity:

Model 1. Keplerian only,

Model 2. Keplerian and quasiperiodic GP, and

Model 3. Keplerian and Matérn-5/2 (M5/2) GP.

Model fits are conducted with all 83 HPF RVs using the pyaneti modeling suite (Barragán et al. 2019, 2022).

All three models fit for a Keplerian orbit with five parameters: orbital period (P_b) , time of inferior conjunction $(T_{0,b})$, RV semiamplitude (K_b) , and parameterized forms of the eccentricity and argument of periastron $(\sqrt{e_b} \sin \omega_* \text{ and } \sqrt{e_b} \cos \omega_*$, respectively). Furthermore, for each set of HPF RV observations, we add a "jitter" term $(\sigma_{\text{HPF}_1} \text{ and } \sigma_{\text{HPF}_2})$ to account for any additional instrumental noise not represented in the measurement uncertainties, as well as zero-point velocity terms $(\gamma_{\text{HPF}_1} \text{ and } \gamma_{\text{HPF}_2})$ to account for any systematic offsets. Models 2 and 3 additionally include GP components with different kernels, as described in Sections 4.5.2 and 4.5.3.

For all models, the parameter posterior distributions are sampled with a Markov Chain Monte Carlo Metropolis—Hasting algorithm as described by Sharma (2017). Each distribution is compiled from 50 independent chains of 200,000 iterations and a thinning factor of 10. Convergence is determined using the Gelman–Rubin statistic, with all chains having values under 1.02 (Gelman & Rubin 1992).

4.5.1. Model 1: Keplerian Only

For Model 1, we perform a Keplerian orbit fit to the RVs for the nine parameters described above. No stellar activity mitigation scheme is adopted in this fiducial fit. Moreover, to search for longer-term accelerations, we also separately carry out two additional fits that model linear and and linear + quadratic terms ($\dot{\gamma}$ and $\ddot{\gamma}$) for Model 1 only.

We impose uniform priors on all Keplerian model parameters. Based on the strong 4 day signal from the periodogram, we adopt $\mathcal{P}(P_b) = \mathcal{U}[0.5, 10.0]$ days and $\mathcal{P}(T_{0,b}) = \mathcal{U}[2458483.0, 2458487.5]$ days as priors for the orbital period and time of transit, respectively. We set the prior on K_b to $\mathcal{P}(K_b) = \mathcal{U}[1.0, 1000.0] \,\mathrm{m\,s^{-1}}$. For the eccentricity parameters, we allow the full range of $\mathcal{P}(\sqrt{e_b} \sin \omega_*) = \mathcal{U}[-1, 1]$ and $\mathcal{P}(\sqrt{e_b} \cos \omega_*) = \mathcal{U}[-1, 1]$, which results in a uniform sampling of $\mathcal{P}(e_b) = \mathcal{U}[0, 1)$ and $\mathcal{P}(\omega_*) = \mathcal{U}[0, 2\pi]$, for e_b and ω_* respectively. For the jitter terms, we adopt modified Jeffreys priors, $\mathcal{J}(1, 100) \,\mathrm{m\,s^{-1}}$, as defined by Equation (16) of Gregory (2005):

$$\mathcal{P}(\sigma; \, \sigma_a, \, \sigma_{\text{max}}) = \frac{1}{\sigma_a + \sigma} \frac{1}{\ln\left[(\sigma_a + \sigma_{\text{max}})/\sigma_a\right]}.$$
 (2)

The modified Jeffreys prior behaves like a uniform prior for $\sigma < \sigma_a$ and a Jeffreys prior for $\sigma > \sigma_a$. The Jeffreys prior is scale invariant in that it treats each decade bin as having equal probability. For the offset terms, we use uniform priors bounded by the minimum and maximum of the RV measurements, $\mathcal{P}(\gamma_{\mathrm{HPF_i}}) = \mathcal{U}[\min(\mathrm{HPF_i}), \max(\mathrm{HPF_i})]$. For the model fits that incorporate long-term trends, we adopt uniform priors of $\mathcal{P}(\dot{\gamma}) = \mathcal{U}[-1, 1] \,\mathrm{km\,s}^{-1}$ day $^{-1}$ and $\mathcal{P}(\ddot{\gamma}) = \mathcal{U}[-1, 1] \,\mathrm{km\,s}^{-1}$ day $^{-2}$.

We report the results of the Model 1 fit in Appendix B. Table B2 summarizes the parameter constraints and Figure B1 displays the best-fit Keplerian signal, 1σ and 3σ confidence intervals, and associated joint posterior distributions in the form of a corner plot. We note that the model fits with linear and quadratic terms are consistent with zero acceleration and return nearly identical solutions. The resulting Bayesian information criterion (BIC; Schwarz 1978; Raftery 1986; Tran et al. 2022) for the Keplerian-orbit only, Keplerian orbit and acceleration, and Keplerian orbit, acceleration, and curvature models are -12.0, -8.2, and -3.8, respectively, which indicate that the data prefer the Keplerian-orbit-only model. Thus, we report only the single-planet model without long-term acceleration or curvature terms.

The median and 1σ posterior values for the Keplerian semiamplitude and orbital period are $K_{b,\mathrm{Model}\;1}=301\pm27~\mathrm{m~s^{-1}}$ and $P_{b,\mathrm{Model}\;1}=3.986^{+0.001}_{-0.001}$ days, respectively. Using our adopted stellar mass, $M_*=0.69\pm0.07~M_{\odot}$ (Section 4.2), we find a minimum mass of $m_b\sin i_{\mathrm{Model}\;1}=1.78^{+0.22}_{-0.21}~M_{\mathrm{Jup}}$ for HS Psc b. The best-fit eccentricity points to a modest value of $e_{b,\mathrm{Model}\;1}=0.18$, although the posteriors are broad and consistent with circular orbits. The rms of the RV residuals after subtracting the best-fit Keplerian curve is $178~\mathrm{m~s^{-1}}$.

The inferred posteriors of the RV jitter terms are $\sigma_{HPF_1, \, \text{Model } 1} = 161.3^{+21.0}_{-24.6} \, \text{m s}^{-1}$ and $\sigma_{HPF_2, \, \text{Model } 1} = 17.4^{+27.2}_{-17.4} \, \text{m s}^{-1}$. The large difference between $\sigma_{HPF_1, \, \text{Model } 1}$ and $\sigma_{HPF_2, \, \text{Model } 1}$ is likely driven by stronger stellar activity during the HPF₁ observations. The evolution of stellar activity over time is evident from the TESS light curves. The amplitude of photometric variability is approximately a factor of 2 greater in Sector 17 compared to Sector 57. As the HPF₁ and HPF₂ RVs are approximately coincident with TESS Sectors 17 and 57, respectively, this evolution could be driving differences between the jitter terms. Furthermore, the lower number and shorter time baseline of the

HPF₂ RVs results in a diminished exploration of the stellar activity. This effect is amplified as a nightly cadence over this short observational window, which results in limited sampling of the stellar rotation period with the HPF₂ observations. When phased to $P_{\rm rot} = 1.086$ days, the HPF₂ RVs cover only roughly one-third of the stellar rotation phase space. This poor phase coverage can artificially dampen activity signals in the HPF₂ measurements, leading to a lower jitter estimate. Altogether these factors suggest that stellar activity is prominent in the RVs and necessitate a mitigation strategy.

4.5.2. Model 2: Keplerian and Quasiperiodic Gaussian Process

In Model 2, we simultaneously fit for a Keplerian signal and a GP model defined by a QP kernel. Under similar assumptions as for photometry (see Section 4.3), QP GPs have been widely leveraged to model stellar activity in RVs (e.g., Haywood et al. 2014; Grunblatt et al. 2015; Faria et al. 2016; Cloutier et al. 2017; Dai et al. 2017). We adopt a GP model with a QP kernel as implemented in pyaneti:

$$k_{\rm QP}(t, t') = A^2 \exp\left(-\frac{(t - t')^2}{2\lambda_e^2} - \frac{\sin^2\left(\frac{\pi(t - t')}{P_{\rm GP}}\right)}{2\lambda_p^2}\right),$$
 (3)

where t and t' represent the pairs of observations in time, and A, λ_e , $P_{\rm GP}$, and λ_p are the same or analogous to A, l, $P_{\rm rot}$, and θ from Equation (1).

We adopt uniform priors on all Keplerian parameters. Based on the results from Model 1, we impose $\mathcal{P}(P_b) = \mathcal{U}[3.5, 4.5]$ days and $\mathcal{P}(T_{0,b} = \mathcal{U}[2458485.0, 2458488.0]$ days as priors for the orbital period and time of transit, respectively. All other priors for planetary parameters are the same as in Model 1.

For the QP kernel hyperparameters, we adopt $\mathcal{P}(A) = \mathcal{U}[0.0,\ 1000.0]$ m s⁻¹, $\mathcal{P}(\lambda_e) = \mathcal{U}[0.01,\ 5.0]$, $\mathcal{P}(\lambda_p) = \mathcal{U}[0.01,\ 5.0]$, and $\mathcal{P}(P_{\text{GP}}) = \mathcal{N}(1.09,\ 0.02)$ days for $A,\ \lambda_e,\ \lambda_p$, and P_{GP} , respectively. This last prior uses the MAP value and $5\times$ the standard deviation of P_{rot} measured from the TESS photometry. This is based on the assumption that the stellar activity signal is starspot driven and will modulate at the stellar rotation period in both the photometric and RV time series (e.g., Aigrain et al. 2012; Tran et al. 2023). The larger range allow the model to explore potential deviations in the rotation period across the large observational window, for instance from midlatitude spots that could produce a spread of periodic signals as a result of differential rotation.

Table B2 and Figure B2 in Appendix B summarizes and displays the results of the Model 2 fit, respectively. The inferred Keplerian semiamplitude and orbital period from Model 2 are $K_{b,\mathrm{Model}\,2}=264^{+84}_{-86}$ m s⁻¹ and $P_{b,\mathrm{Model}\,2}=3.986^{+0.005}_{-0.024}$ days. This corresponds to a minimum mass of $m_b \sin i_{\mathrm{Model}\,2}=1.46^{+0.54}_{-0.43}$ M_{Jup} . The eccentricity is effectively unconstrained, as the posterior spans all possible values, although there is a slight preference for low eccentricities with $e_{b,\mathrm{Model}\,2}=0.25^{+0.19}_{-0.25}$. The inferred RV jitter terms are $\sigma_{\mathrm{HPF_1,\,Model}\,2}=8.0^{+10.7}_{-8.0}$ m s⁻¹ and $\sigma_{\mathrm{HPF_2,\,Model}\,2}=8.1^{+11.7}_{-8.1}$ m s⁻¹. The rms of RV residuals for Model 2 is 108 m s⁻¹.

4.5.3. Model 3: Keplerian and Matérn-5/2 Gaussian Process

For Model 3, we perform a similar joint Keplerian-plus-GP model fit as Model 2, but with a GP defined by a Matérn–5/2 (M5/2) kernel instead of a QP kernel. Our goal is to assess how

changes to the GP stellar activity model can impact the inferred planetary parameters. Furthermore, this change allows us to account for the possibility that the stellar activity signals manifest differently in the RVs as compared to the TESS photometry. The Matérn family of kernels are also widely adopted in GP regression to model more stochastic behavior. GP models incorporating the M5/2 kernel and its derivative have been found to match stellar activity in solar RV data reasonably (Gilbertson et al. 2020).

We apply a GP model with a M5/2 kernel as defined in pyaneti:

$$k_{\text{M5/2}}(t, t') = A^2 \left(1 + t_{5/2} + \frac{t_{5/2}^2}{3} \right) \exp(-t_{5/2}),$$
 (4)

with $t_{5/2} \equiv \sqrt{5} |t - t'| \lambda^{-1}$, where λ is the length of local variations.

We adopt uniform priors for all parameters in the joint Model 3 fit. For the planetary parameters, we impose the same priors as in Model 2. For the M5/2 kernel hyperparameters, we choose $\mathcal{P}(A) = \mathcal{U}[0.0, 1000.0]$ m s⁻¹ for A and $\mathcal{P}(\lambda) = \mathcal{U}[0.001, 10.0]$ for λ .

Table 2 details the results of the Model 3 fit. Figure 3 displays the best-fit phased RV curves and posterior distributions of the planetary and M5/2 kernel parameters. For Model 3, the inferred Keplerian semiamplitude is $K_{b,\mathrm{Model 3}} = 268^{+91}_{-92}$ m s⁻¹, which corresponds to a minimum planetary mass of $m_b \sin i_{\mathrm{Model 3}} = 1.46^{+0.56}_{-0.44}$ M_{Jup} . The orbital period is $P_{b,\mathrm{Model 3}} = 3.986^{+0.044}_{-0.003}$ days. Similar to Model 2, the eccentricity is unconstrained with some preference for low values $(e_{b,\mathrm{Model 3}} = 0.27^{+0.21}_{-0.27})$ and the RV jitter terms are $\sigma_{\mathrm{HPF_b,\,Model 3}} = 8.2^{+11.6}_{-8.2}$ m s⁻¹ and $\sigma_{\mathrm{HPF_b,\,Model 3}} = 8.2^{+11.6}_{-8.2}$ m s⁻¹. The rms of the Model 3 RV residuals is 99 m s⁻¹.

4.5.4. Model Comparison, Gaussian Process Cross-validation, and Adopted Parameters

All inferred posteriors for the planetary and instrumental parameters are consistent among the three models within 1σ except for the HPF $_1$ RV jitter term. The posterior values of σ_{HPF_1} are similar for both Models 2 and 3, which are reduced by a factor of approximately 20 compared to the inferred Model 1 values. This suggests that the higher Model 1 σ_{HPF_1} values are driven by correlated stellar activity signals as both GP models are able to remove this additional scatter. Furthermore, Models 2 and 3, which employ GPs with different kernel choices, yield nearly identical planetary parameters. This provides evidence that the GP models are identifying similar correlated signals and are robust against kernel selection, which can affect the inferred planetary properties (e.g., Benatti et al. 2021).

The GP models also decrease the rms of the RV residuals. The residual rms values are 178, 109, and 99 m s⁻¹ for Models 1, 2, and 3, respectively. Altogether the lower overall residuals, the reduced σ_{HPF_1} parameter, and the consistent planetary values suggest that the GP models are effectively mitigating stellar activity contributions to the RVs of HS Psc.

Finally, the uncertainties in the RV semiamplitudes and eccentricities for Models 2 and 3 are larger than for Model 1. The 1σ uncertainties of Models 2 and 3 increase by a factor of approximately 3 for K_b and 2 for e_b as compared to Model 1. The lower Model 1 uncertainties can be attributed to the large planetary amplitude, long time baseline, and high number of

Table 2
Parameter Priors and Posteriors from the Keplerian and Matérn–5/2 GP Fit (Model 3) to the HPF Radial Velocities of HS Psc

Parameter	Prior ^a	MAP ^b	Median $\pm 1\sigma$	
	Fitted Param	eters		
	Keplerian and Instrume	ntal Parameters		
P_b (day)	U[3.5, 4.5]	3.986	$3.986^{+0.044}_{-0.003}$	
$T_{0,b}$ (day)	$\mathcal{U}[2458485.0, 2458488.0]$	2458486.565	$2458486.422_{-0.523}^{+0.429}$	
$K_b \text{ (m s}^{-1})$	U[1.0, 1000.0]	281.6	268 ⁺⁹¹ ₋₉₂	
$\sqrt{e_b} \sin \omega_*$	$\mathcal{U}[-1,1]$	0.10	$0.01_{-0.50}^{+0.45} \\ -0.10_{-0.39}^{+0.38} \\ 8.2_{-8.2}^{+11.2} \\ 8.2_{-8.2}^{+0.047} \\ -0.037_{-0.051}^{+0.047}$	
$\sqrt{e_b}\cos\omega_*$	$\mathcal{U}[-1,1]$	-0.38		
$\sigma_{\text{HPF}_1} \text{ (m s}^{-1})$	$\mathcal{J}(1, 100)$	0.1		
$\sigma_{HPF_2} \text{ (m s}^{-1}\text{)}$	$\mathcal{J}(1, 100)$	0.4		
$\gamma_{\mathrm{HPF_1}} \ (\mathrm{km \ s^{-1}})$	U[-1.0922, 0.9655]	-0.025		
$\gamma_{\rm HPF_2} \ ({\rm km\ s}^{-1})$	$\mathcal{U}[-0.8858, 1.0037]$	0.076	$0.068^{+0.090}_{-0.088}$	
-	M5/2 GP Kernel Hyp	perparameters		
$A \text{ (m s}^{-1})$	$\mathcal{U}[0.0,1000.0]$	139.5	$187.2^{+41.1}_{-55.6}$	
λ	$\mathcal{U}[0.001,\ 10.0]$	0.02	$0.09^{+0.04}_{-0.08}$	
	Derived Parar	neters		
$m_b \sin i^{\rm c} (M_{\rm Jup})$		1.71	$1.46^{+0.56}_{-0.44}$	
a_b (au)		0.0436	$0.0435^{+0.0017}_{-0.0017}$	
$T_{\text{peri,b}}$ (day)		2458487.21	$2458486.71_{-0.91}^{+1.46}$	
e_b		0.16	$0.27^{+0.21}_{-0.27}$	
ω_* (°)		165.30	$176.25^{+101.88}_{-102.74}$	

Notes.

RV observations. However, the posterior width may not fully capture the effects of stellar activity, which are not explicitly built into the model. These larger uncertainties present in Models 2 and 3 better reflect the difficulty of detecting and appropriately characterizing a young planet candidate such as HS Psc b.

Altogether we find that a joint GP model better predicts the HPF RVs compared to a Keplerian-only model. However, GP regression can be susceptible to overfitting (e.g., Aigrain & Foreman-Mackey 2023; Blunt et al. 2023), leading to systematic biases that affect the interpretation of a planetary signal. This is particularly true for young systems where stellar activity signals are large.

To assess the possibility of Models 2 and 3 overfitting the data, we apply a cross-validation, or "train-test-split," test as described in Blunt et al. (2023). Cross-validation is a procedure designed to test the predictive performance of a model (Gelfand et al. 1992; Aigrain & Foreman-Mackey 2023). As implemented in Blunt et al. (2023), a validation sample is first constructed by splitting the data into training and test sets, which are comprised of 80% and 20% of the data, respectively. The model is then conditioned on the training set and the best-fit model predictions at the times of the test set are compared to the test set values. If the predictions produce similar residuals for the withheld data as with the conditioned data, then the model is predictive and can be considered robust against overfitting.

We randomly withhold 17 RVs out of the 83 observations (amounting to 20% of the data) and conduct this cross-validation test for both Models 2 and 3. Figure 4 displays the training and test data sets, best-fit model predictions, and fit residuals from this cross-validation test for Models 2 and 3. For both models, the residuals of the test set have consistent structure and spread with the training set residuals. This test is repeated twice more with different data split variations. The results in all three instances are consistent. We interpret the similarity between the residuals of the training and test sets as evidence supporting the predictive nature of the best-fit models, indicating that Models 2 and 3 do not overfit the RV data.

To determine which model is favored by the data, we further evaluate comparison metrics between Models 1, 2, and 3. Table 3 reports different model selection criteria for each of the three models, including the BIC, both the uncorrected and corrected Akaike information criterion (AIC and AIC $_c$, respectively; Akaike 1998; Tran et al. 2022) and the Akaike weights (Akaike 1981; Burnham & Anderson 2004; Liddle 2007). The BIC comparison suggests that there is strong evidence in favor of Model 3 (Δ BIC > 5 against Models 1 and 2). The Akaike weights, or relative likelihoods, also prefer Model 3 over Models 1 and 2 (92% favorability).

The consistent inferred parameters, reduced residual rms values, cross-validation tests, and model selection criteria all indicate that Model 3 performs the best at robustly detecting the Keplerian signal and modeling the correlated stellar activity signals. As a result, we adopt the results from Model 3, the

^a U[a, b] refers to the uniform distribution bounded by a and b. $\mathcal{J}(a, b)$ refers to the modified Jeffreys prior as defined in Equation (6) of Gregory (2005), $\mathcal{P}(x) = 1/(a+x) \cdot 1/\ln[(a+b)/a]$.

^b Map refers to the maximum a posteriori value.

^c Planetary mass is derived assuming a stellar mass of $M_* = 0.69 \pm 0.07~M_{\odot}$.

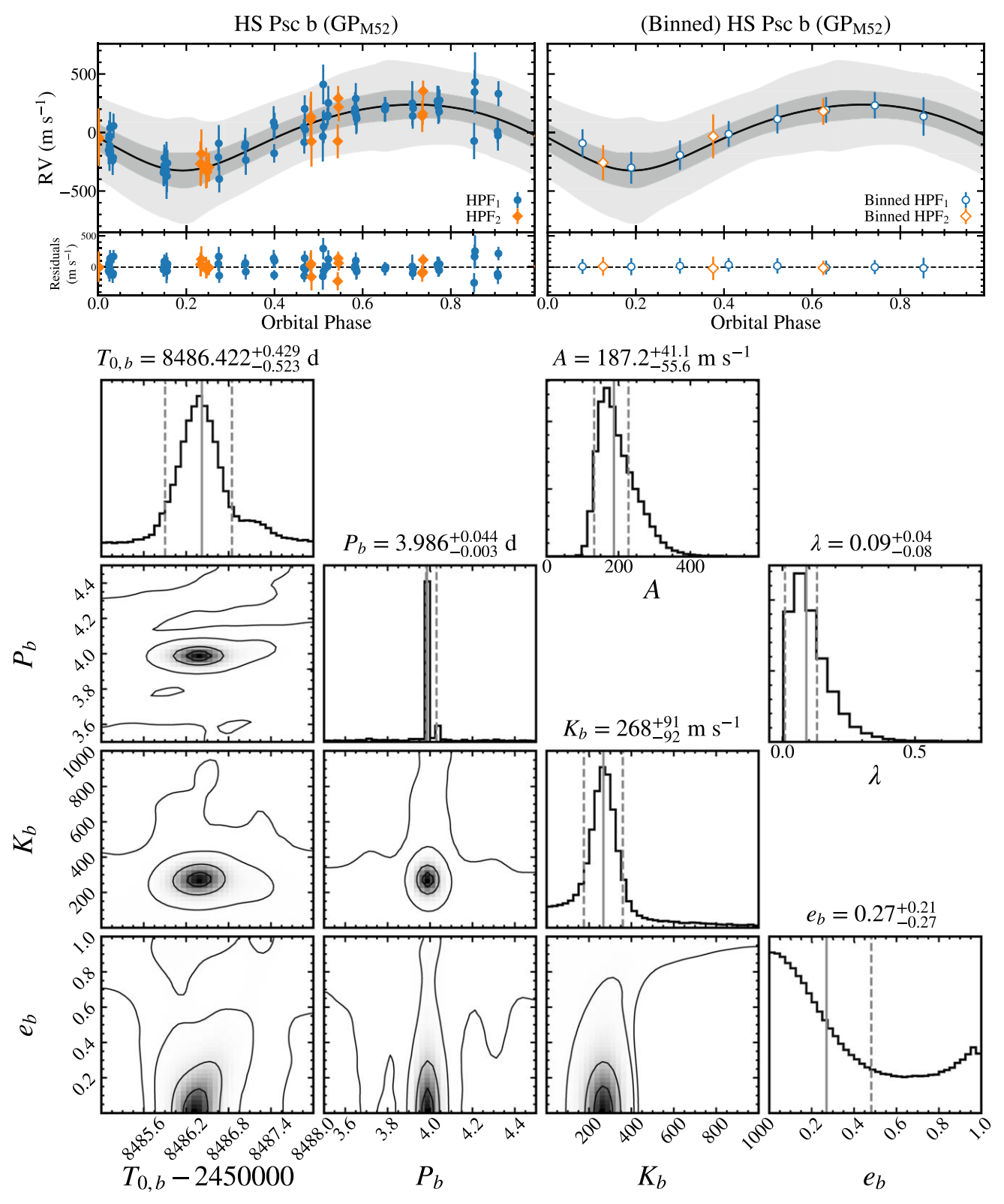


Figure 3. Top: RV curve of HS Psc b phase folded to the best-fit orbital period from Model 3. The blue and orange points denote the two different observing seasons, HPF₁ and HPF₂, respectively, and the best-fit RV model is shown as the solid black line. The fit residuals are plotted in the lower panels. The colored error bars are nominal RV errors and the gray error bars include the systematic jitter terms. 1σ and 3σ confidence intervals are plotted as gray shaded regions. The right panel displays the same best-fit orbit with the phased RV points representing median values in bins of ≈ 0.1 and ≈ 0.2 of the phase for the HPF₁ and HPF₂ RVs, respectively. The bottom panels display the joint posterior distributions of $T_{0,b}$, P_b , K_b , and e_b from the Model 3 fit of HS Psc b. The diagonal panels show the marginalized distribution for each parameter. The upper right panels show the marginalized distributions for the M5/2 kernel parameters.

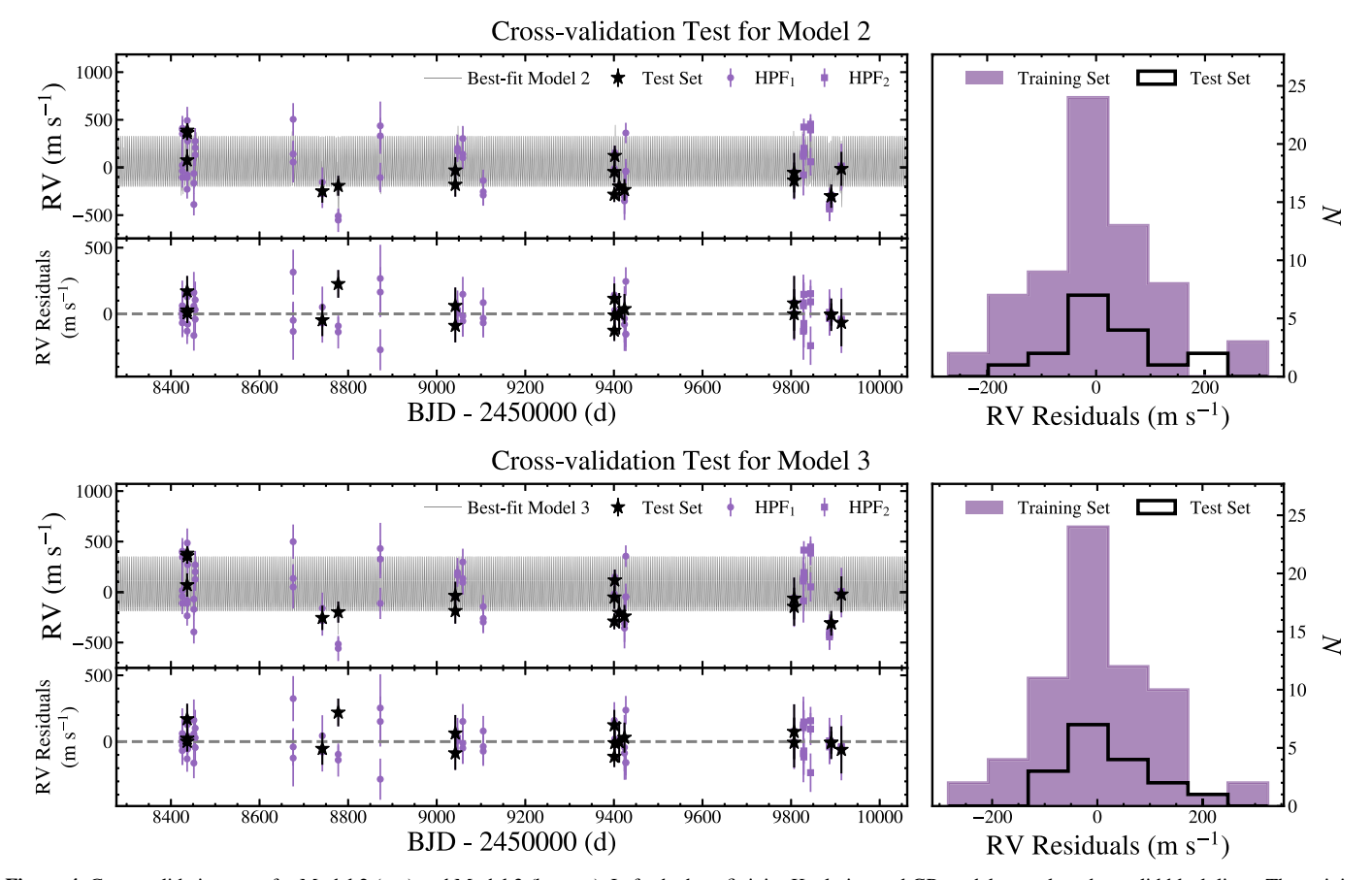


Figure 4. Cross-validation tests for Model 2 (top) and Model 3 (bottom). Left: the best-fit joint Keplerian and GP models are plotted as solid black lines. The training and test RV data sets are displayed as purple points and black stars, respectively. The residuals between the models and both data sets are displayed on the bottom. Right: the distributions of RV residuals for the training and test data sets are plotted in purple and black, respectively. The range and structure of the residuals are consistent between the training and test sets, supporting the predictive power of the best-fit models and providing evidence against overfitting.

Table 3
Metrics for the Best-fit Model Comparison

Model	In $\mathcal L$	k	N	BIC	AIC	AIC_c	Akaike Weight
Model 1 (Keplerian only)	25.92	9	83	-12.07	-33.84	-31.37	< 0.01
Model 2 (Keplerian + QP GP)	35.48	13	83	-13.51	-44.95	-39.68	0.08
Model 3 (Keplerian $+$ M5/2 GP)	35.09	11	83	-21.57	-48.18	-44.46	0.92

Note. Lower metric values indicate a preferred model. The model in bold (Keplerian-plus-M5/2 GP) is adopted as the overall best-fit solution.

joint Keplerian and M5/2 GP model, as the most appropriate values for HS Psc b.

5. Discussion

5.1. Exclusion of a Low-inclination Brown Dwarf or Stellar Companion

RV observations alone cannot measure the true mass of a Keplerian signal. RV surveys are thus susceptible to false positive scenarios in which a BD or stellar companion on a face-on orbit masquerades as a planet (e.g., Wright et al. 2013). In Section 4.5, we report a minimum mass of $m \sin i_* = 1.46$ $M_{\rm Jup}$. For HS Psc b to have a true mass larger than the BD limit ($\geqslant 13~M_{\rm Jup}$), its orbital inclination must be $i \leqslant 6.4^\circ$. Assuming an isotropic distribution for inclinations, the a priori probability of this scenario is $P \approx 0.64\%$. For a stellar mass companion ($\geqslant 75~M_{\rm Jup}$), this probability decreases to $P \approx 0.019\%$. However, these probabilities only reflect the chances of a false

positive planet signal for this particular star and do not take into account our broader survey size; the larger the survey, the more false positive planets should be found. Binomial statistics can be used to correct for this sample size by determining the probability of a success (planet) given an underlying rate (the false positive probability) and a sample size (104 stars, in this case). This result will assume that each star in the sample has a short-period stellar or substellar companion, so the resulting probability needs to be multiplied by the actual occurrence rate of these companions.

Combining this probability of an inclined BD, binomial statistics based on our survey, and a conservative estimate of 1% for the occurrence rate of BDs, we calculate the probability of observing at least one false positive event in our sample of 104 systems as $P_{\rm FP} = 0.48\%$. This false positive rate is an upper limit as the occurrence rate of close-in ($a \lesssim 5$ au) BDs is $\lesssim 1\%$ (e.g., Grether & Lineweaver 2006; Sahlmann et al. 2011; Santerne et al. 2016) and even lower at closer separations

 $(P \lesssim 100 \, \mathrm{days})$; Ma & Ge 2014; Csizmadia et al. 2015; Ranc et al. 2015; Kiefer et al. 2019). The true probability of a false alarm scenario is therefore likely to be <0.48%. Moreover, we note that the stellar inclination is likely high (Section 4.3) and hot Jupiters around cool stars usually have low obliquities (e.g., Winn et al. 2010; Albrecht et al. 2022), so it would be unusual for the planet inclination to differ substantially from 90°. Based on these estimates, we confidently exclude the possibility that HS Psc b is a BD or star on an inclined orbit.

5.2. Timescales for Tidal Circularization and High-eccentricity Migration

As a young hot Jupiter, HS Psc b could offer rare constraints on the timescales of different migration processes such as tidal circularization and high-eccentricity migration. Tidal interactions between close-in planets and their host stars lead to an exchange of angular momentum and, as a result, evolution in orbital separation and eccentricity. The characteristic timescale for this mechanism is typically short compared to the characteristic age of several gigayears for field stars. A general form for the tidal circularization timescale is given by Equation (3) of Adams & Laughlin (2006):

$$\tau_{\rm cir} \approx 1.6 \, {\rm Gyr} \left(\frac{Q_p}{10^6}\right) \left(\frac{m_p}{M_{\rm Jup}}\right) \times \left(\frac{M_*}{M_\odot}\right)^{-3/2} \left(\frac{r_p}{R_{\rm Jup}}\right)^{-5} \left(\frac{a}{0.05 \, {\rm au}}\right)^{13/2}, \tag{5}$$

where Q_P is the tidal quality factor, generally 10^5 – 10^6 , m_p and r_p are the planetary mass and radius, respectively, M_* is the stellar host mass, and a is the orbital separation. This relation holds for systems where the planetary orbital period is greater than the stellar rotational period (Goldreich & Soter 1966; Jackson et al. 2008). However, HS Psc b operates in the supersynchronous rotation regime, where $P_{\rm orb} > P_{\rm rot}$ (Ferraz-Mello et al. 2008). In this state, the assumptions in Equation (5) break down and tidal forces operate less efficiently. As a result, circularization timescales estimated by Equation (5) should be treated as lower limits (Jackson et al. 2008).

Coupled with the age of the system, this lower limit can provide us with a sense of the minimum time it should take for a planet like HS Psc b to tidally circularize if it had a high eccentricity after migrating to its current orbital distance. Adopting the median values reported in this work and assuming radii of $\{1.0, 1.25, 1.5\}$ $R_{\rm Jup}$, the ranges of tidal circularization timescales of HS Psc b are $\tau_{\rm cir} = \{0.18-1.79, 0.09-0.89, 0.05-0.48\}$ Gyr.

These estimates suggest the earliest timescale for tidal circularization is on the order of several tens of megayears. This means that if the current eccentricity of HS Psc b is zero, then if it migrated recently through high-eccentricity migration, the earliest that process could have occurred was a few tens of megayears ago. It could also have migrated this way soon after formation, setting an upper limit to this process of ≈ 130 Myr. A low eccentricity is also consistent with disk migration early on. On the other hand, if HS Psc b currently has a modest or

high eccentricity, then it should still be in the process of circularizing and high-eccentricity migration could have occurred at any point in the planet's history.

We stress that while the eccentricity posteriors of the adopted model (Model 3) prefer lower values, there is power across all eccentricities and this parameter is not well constrained. Follow-up RV observations are needed to rule out higher eccentricities more confidently and better constrain the evolutionary history and migration timescale of HS Psc b. Irrespective of the specific timing or channel, the discovery of HS Psc b implies that HJs can form or migrate to their current locations by 130 Myr.

5.3. Future Observations

Optical RV observations can further validate and characterize HS Psc b. Modulations arising from the presence of starspots are wavelength dependent; RV amplitudes of starspot-driven variability have been shown to be higher in the optical than in the NIR by a factor of ≈ 2 for systems of this age (e.g., Prato et al. 2008; Mahmud et al. 2011; Baileyet al. 2012; Crockett et al. 2012; Gagné et al. 2016; Tran et al. 2021). Confirming that the RV amplitude, orbital period, and orbital phase of optical RVs are consistent with the NIR HPF observations would further support the planetary nature of HS Psc b. Additional RVs can also be used to search for other companions, such as smaller closer-in or more distant giant planets, to inform further the formation and migration of the system. Moreover, more precise optical RVs can refine the eccentricity of HS Psc b and establish whether it is actively undergoing tidal circularization.

6. Summary

We have presented the discovery and characterization of a young hot Jupiter candidate orbiting a member of the 133^{+15}_{-20} Myr AB Dor moving group as part of the Epoch of Giant Planet Migration planet search program. Below, we summarize our main conclusions.

- We obtained 83 NIR RVs of HS Psc with HPF at the HET. Using SERVAL-based least-squares matching and SpecMatch-Emp-based empirical spectral matching algorithms, we extract the relative RVs, dLWs, CRXs, and Ca II IRT line indices.
- 2. We derive an effective temperature of $T_{\rm eff} = 4203 \pm 116$ K, a metallicity of $[{\rm Fe/H}] = -0.05 \pm 0.09$ dex, a surface gravity of $\log g = 4.66 \pm 0.03$ dex, and a stellar projected rotational velocity of $v \sin i_* = 29.7 \pm 3.1$ km s⁻¹ for HS Psc. We infer a stellar mass of $M_* = 0.69 \pm 0.07$ M_{\odot} and radius of $R_* = 0.65 \pm 0.07$ R_{\odot} for HS Psc using the ARIADNE and isochrones packages. These values are consistent with its spectral type of K7V, stellar age, and previous literature values.
- 3. Our HPF RVs over 4 yr reveal a periodicity at P=3.99 days. This period is not commensurate with an integer harmonic of the stellar rotation period measured from TESS photometry ($P_{\rm rot}=1.086\pm0.003$ days). Furthermore, these RV measurements do not correlate significantly with associated activity indicators, supporting a planetary origin for the observed signal.
- 4. A joint Keplerian and M5/2 GP stellar activity model fit to the HPF RVs yields a minimum mass of $m_b \sin i = 1.46^{+0.57}_{-0.44} M_{\rm Jup}$, an orbital period of $P_b = 3.986^{+0.044}_{-0.003}$ days,

 $[\]overline{^{16}}$ Giant plants are inflated at young ages, then cool and contract over time. Based on the mass (1–2 $M_{\rm Jup}$) and age (\approx 100 Myr) of HS Psc b, hot-star-giant planet evolutionary models predict a radius \sim 1.2 $R_{\rm Jup}$ (e.g., Burrows et al. 2001; Baraffe et al. 2003; Morley et al. 2024).

- and a broad eccentricity constraint with a slight preference for low values. No evidence of a longer-term acceleration is evident. HS Psc b is unlikely to be a BD or star on a face-on orbit.
- 5. As a young, close-in giant planet, HS Psc b may have undergone high-eccentricity tidal migration. If so, we estimate a lower limit of several tens of megayears for the tidal circularization timescale of HS Psc b. The age of HS Psc places an upper limit on the migration timescale of ≈130 Myr. Disk migration is also possible if HS Psc b has a low eccentricity. A modest or high eccentricity would imply that it is still undergoing circularization. Additional high-precision RV observations will help confirm HS Psc b, refine the orbit and minimum mass, and constrain its orbital evolutionary history.

HS Psc b joins only a small handful of other hot Jupiter candidates that have both robust age constraints and planetary (minimum) mass measurements. HS Psc b is an excellent target for future observations with precision optical and IR spectrographs. If confirmed with follow-up RVs, HS Psc b will be one of the youngest hot Jupiters discovered to date.

Acknowledgments

The authors would like to thank Marvin Morgan, Kyle Franson, and Adam Kraus for insightful discussions on the high-eccentricity tidal migration, orbital circularization, and thermal evolution of close-in giant planets. The authors would also like to thank Chad Bender, Steven Janowiecki, Greg Zeimann, the HPF team, and all the resident astronomers and telescope operators at the HET for supporting these observations and data processing. The authors are grateful to the referee for their helpful comments, which improved the quality of this manuscript.

Q.H.T. and B.P.B. acknowledge the support from a NASA FINESST grant (80NSSC20K1554). B.P.B. acknowledges support from the National Science Foundation grant AST-1909209, NASA Exoplanet Research Program grant 20-XRP20_2-0119, and the Alfred P. Sloan Foundation. G.S. acknowledges support provided by NASA through the NASA Hubble Fellowship grant HST-HF2-51519.001-A awarded by the Space Telescope Science Institute, which is operated by the Association of Universities for Research in Astronomy, Inc., for NASA, under contract NAS5-26555.

These results are based on observations obtained with the Habitable-zone Planet Finder (HPF) Spectrograph on the Hobby–Eberly Telescope (HET). The HPF team acknowledges support from NSF grants AST-1006676, AST-1126413, AST-1310885, AST-1517592, AST-1310875, ATI 2009889, ATI-2009982, and AST-2108512, and the NASA Astrobiology Institute (NNA09DA76A) in the pursuit of precision RVs in the NIR. The HPF team also acknowledges support from the Heising-Simons Foundation via grant 2017-0494. The Hobby–Eberly Telescope is a joint project of the University of Texas at Austin, the Pennsylvania State University, Ludwig-Maximilians-Universität München, and Georg-August Universität Gottingen. The HET is named in honor of its principal benefactors, William P. Hobby and Robert E. Eberly. The HET collaboration acknowledges the support and resources from the

Texas Advanced Computing Center. Computations for this research were also performed on the Pennsylvania State University's Institute for Computational and Data Sciences Advanced CyberInfrastructure (ICDS-ACI, now known as Roar), including the CyberLAMP cluster supported by NSF grant MRI1626251.

We would like to acknowledge that the HET is built on indigenous land. Moreover, we would like to acknowledge and pay our respects to the Carrizo and Comecrudo, Coahuiltecan, Caddo, Tonkawa, Comanche, Lipan Apache, Alabama-Coushatta, Kickapoo, Tigua Pueblo, and all the American Indian and indigenous people and communities who have been or have become a part of these lands and territories in Texas, here on Turtle Island.

This paper includes data collected by the TESS mission. Funding for the TESS mission is provided by the NASA's Science Mission Directorate. This work presents results from the European Space Agency (ESA) space mission Gaia. Gaia data are being processed by the Gaia Data Processing and Analysis Consortium (DPAC). Funding for the DPAC is provided by national institutions, in particular the institutions participating in the Gaia MultiLateral Agreement (MLA).

This research has made use of the VizieR catalog access tool, CDS, Strasbourg, France (doi:10.26093/cds/vizier). The original description of the VizieR service was published in 2000, A&AS 143, 23. This publication makes use of data products from the Two Micron All Sky Survey (2MASS), which is a joint project of the University of Massachusetts and the Infrared Processing and Analysis Center/California Institute of Technology, funded by the National Aeronautics and Space Administration and the National Science Foundation. This publication makes use of data products from the Wide-field Infrared Survey Explorer, which is a joint project of the University of California, Los Angeles, and the Jet Propulsion Laboratory/California Institute of Technology, funded by the National Aeronautics and Space Administration. Facilities: HET (HPF) and TESS.

Software: ARIADNE (Vines & Jenkins 2022), astropy (Astropy Collaboration et al. 2013, 2018, 2022), astroquery (Ginsburg et al. 2019), barycorrpy (Kanodia & Wright 2018), celerite2 (Foreman-Mackey et al. 2017; Foreman-Mackey 2018), dustmaps (Green 2018), dynesty (Higson et al. 2019; Speagle 2020; Koposov et al. 2023), HxRGproc (Ninan et al. 2018), isochrones (Morton 2015), lightkurve (Lightkurve Collaboration et al. 2018), matplotlib (Hunter 2007), MultiNest (Feroz et al. 2009, Feroz et al. 2019), numpy (van der Walt et al. 2011), pandas (McKinney 2010), pyaenti (Barragán et al. 2019, 2022), PyMultiNest (Buchner et al. 2014), scipy (Virtanen et al. 2020), and SERVAL (Zechmeister et al. 2018).

Appendix A HPF Radial Velocities and Activity Indicators

Table A1 lists the measured relative HPF RVs and associated stellar activity indicators of HS Psc b. See Section 3.2 for details.

Table A1
Relative HPF Radial Velocities, Activity Indicators (dLW and CRX), and Line Indices for the Ca II Infrared Triplet Line Measurements and Uncertainties

BJD _{TDB} (day)	RV (m s ⁻¹)	dLW (m2 s-2)	CRX (m s ⁻¹ Np ⁻¹)	Ca II IRT 1	Ca II IRT 2	Ca II IRT 3	Instrument
2458425.6292	-17.5 ± 190.0	3346.0 ± 1061.7	183.4 ± 234.8	0.919 ± 0.005	0.866 ± 0.006	0.820 ± 0.005	HPF ₁
2458425.6333	-144.2 ± 108.2	1691.0 ± 708.1	100.1 ± 131.0	0.882 ± 0.005	0.854 ± 0.007	0.788 ± 0.005	HPF_1
2458425.6371	-76.3 ± 75.2	1424.3 ± 973.8	1.2 ± 95.3	0.875 ± 0.005	0.788 ± 0.007	0.771 ± 0.006	HPF_1
2458425.8566	371.1 ± 130.4	251.4 ± 646.0	-103.6 ± 161.5	0.907 ± 0.004	0.859 ± 0.005	0.794 ± 0.004	HPF_1
2458425.8605	358.5 ± 73.1	1613.4 ± 592.2	-2.7 ± 93.6	0.875 ± 0.005	0.805 ± 0.007	0.771 ± 0.005	HPF_1
2458425.8644	313.5 ± 146.2	-379.1 ± 762.8	-112.3 ± 182.3	0.882 ± 0.004	0.840 ± 0.005	0.779 ± 0.004	HPF_1
2458436.6067	-146.1 ± 67.9	-791.0 ± 722.2	18.4 ± 86.0	0.875 ± 0.005	0.845 ± 0.006	0.774 ± 0.005	HPF_1
2458436.6107	-268.5 ± 97.6	-697.6 ± 751.3	-159.5 ± 104.2	0.899 ± 0.004	0.870 ± 0.005	0.803 ± 0.004	HPF_1
2458436.6146	36.2 ± 115.6	707.6 ± 803.3	90.6 ± 141.7	0.898 ± 0.004	0.838 ± 0.006	0.790 ± 0.005	HPF_1
2458436.6186	-116.9 ± 137.6	305.5 ± 814.0	84.5 ± 169.4	0.925 ± 0.004	0.887 ± 0.006	0.831 ± 0.005	HPF_1
2458436.8202	322.8 ± 75.8	543.6 ± 512.2	14.5 ± 96.4	0.971 ± 0.004	0.935 ± 0.006	0.870 ± 0.004	HPF_1
2458436.8241	347.9 ± 72.0	119.3 ± 688.4	-76.4 ± 86.7	0.910 ± 0.004	0.871 ± 0.005	0.821 ± 0.004	HPF ₁
2458436.8280	452.5 ± 143.9	907.0 ± 866.1	-133.9 ± 177.4	0.882 ± 0.005	0.855 ± 0.006	0.775 ± 0.005	HPF_1
2458437.8224	308.3 ± 95.8	892.7 ± 301.8	-111.5 ± 113.1	0.887 ± 0.005	0.813 ± 0.007	0.782 ± 0.006	HPF ₁
2458437.8263	332.5 ± 124.2	748.9 ± 714.4	-183.9 ± 139.3	0.889 ± 0.004	0.847 ± 0.005	0.787 ± 0.004	HPF ₁
2458437.8303	237.5 ± 93.1	115.4 ± 721.8	40.3 ± 116.4	0.896 ± 0.004	0.849 ± 0.005	0.792 ± 0.004	HPF_1
2458437.8343	331.4 ± 92.2	1069.8 ± 412.0	-54.7 ± 114.5	1.048 ± 0.006	1.023 ± 0.008 0.867 ± 0.005	0.925 ± 0.007	HPF_1
2458451.7777 2458451.7816	-204.3 ± 113.8	990.0 ± 972.6 -590.1 \pm 1007.4	-92.5 ± 139.6	0.910 ± 0.004 0.934 ± 0.004		0.815 ± 0.004 0.834 ± 0.004	HPF_1
	-103.0 ± 155.9	-390.1 ± 1007.4 791.6 ± 1006.3	358.8 ± 132.0 90.4 ± 139.7		0.887 ± 0.005		HPF_1
2458451.7856 2458454.7769	-428.4 ± 114.5 166.9 ± 101.7	-474.6 ± 1299.3	90.4 ± 139.7 191.3 ± 101.7	0.888 ± 0.004 0.926 ± 0.005	$\begin{array}{c} 0.820 \pm 0.005 \\ 0.864 \pm 0.007 \end{array}$	$\begin{array}{c} 0.785 \pm 0.004 \\ 0.811 \pm 0.006 \end{array}$	HPF_1 HPF_1
2458454.7709	92.0 ± 113.6	-474.0 ± 1299.3 260.6 ± 933.4	-11.8 ± 145.8	0.925 ± 0.005 0.925 ± 0.005	0.892 ± 0.007	0.811 ± 0.000 0.820 ± 0.006	HPF_1
2458454.7848	235.3 ± 138.5	73.3 ± 569.6	-30.7 ± 175.6	0.923 ± 0.003 0.898 ± 0.004	0.892 ± 0.007 0.843 ± 0.005	0.820 ± 0.000 0.782 ± 0.004	HPF_1
2458675.9378	16.3 ± 213.7	-985.5 ± 1256.5	-30.7 ± 175.0 307.4 ± 245.5	1.055 ± 0.004	1.039 ± 0.009	0.782 ± 0.004 0.951 ± 0.007	HPF_1
2458675.9417	465.5 ± 170.0	-983.3 ± 1230.3 292.4 ± 1314.9	48.0 ± 220.3	0.943 ± 0.004	0.871 ± 0.006	0.822 ± 0.005	HPF_1
2458675.9456	101.6 ± 141.2	528.5 ± 351.9	250.5 ± 153.9	0.945 ± 0.004 0.905 ± 0.004	0.859 ± 0.005	0.822 ± 0.003 0.800 ± 0.004	HPF_1
2458741.7631	-288.4 ± 120.9	469.4 ± 790.5	-88.9 ± 151.6	0.936 ± 0.004	0.895 ± 0.005	0.828 ± 0.004	HPF_1
2458741.7669	-193.6 ± 154.9	-719.7 ± 1244.8	-222.8 ± 177.5	0.930 ± 0.004 0.934 ± 0.004	0.892 ± 0.006	0.834 ± 0.005	HPF_1
2458741.7709	-317.5 ± 147.8	-320.3 ± 1059.5	-91.0 ± 183.3	0.939 ± 0.005	0.893 ± 0.006	0.819 ± 0.005	HPF_1
2458777.6734	-592.2 ± 124.7	2669.3 ± 1018.0	89.2 ± 153.8	0.926 ± 0.003	0.868 ± 0.005	0.802 ± 0.003	HPF_1
2458777.6773	-548.6 ± 66.8	1594.7 ± 977.1	79.2 ± 78.2	0.900 ± 0.004	0.849 ± 0.005	0.796 ± 0.004	HPF_1
2458777.6812	-231.8 ± 104.7	1082.5 ± 1515.2	-106.4 ± 126.6	0.867 ± 0.006	0.850 ± 0.008	0.765 ± 0.007	HPF ₁
2458872.6197	-145.7 ± 155.1	-746.9 ± 1406.9	-309.3 ± 155.1	0.882 ± 0.006	0.849 ± 0.008	0.766 ± 0.006	HPF_1
2458872.6237	292.3 ± 189.1	1433.5 ± 1734.1	-375.9 ± 188.7	0.899 ± 0.004	0.855 ± 0.005	0.803 ± 0.004	HPF_1
2458872.6276	397.6 ± 254.4	-1401.2 ± 1603.1	246.2 ± 310.5	0.969 ± 0.005	0.948 ± 0.006	0.863 ± 0.005	HPF_1
2459041.9448	-83.1 ± 107.6	-532.0 ± 899.8	-40.6 ± 136.7	0.896 ± 0.004	0.872 ± 0.006	0.796 ± 0.004	HPF_1
2459041.9488	-69.4 ± 138.0	313.3 ± 706.2	64.5 ± 174.8	0.899 ± 0.006	0.835 ± 0.008	0.788 ± 0.007	HPF_1
2459041.9527	-220.0 ± 126.1	100.0 ± 1284.0	-97.0 ± 158.9	0.903 ± 0.004	0.869 ± 0.005	0.802 ± 0.004	HPF_1
2459046.9227	131.9 ± 86.2	146.7 ± 833.5	102.0 ± 100.9	0.909 ± 0.003	0.868 ± 0.004	0.800 ± 0.003	HPF_1
2459046.9266	161.5 ± 142.5	1720.4 ± 934.7	347.5 ± 113.8	1.073 ± 0.006	1.023 ± 0.008	0.959 ± 0.006	HPF_1
2459046.9305	141.9 ± 87.0	-32.9 ± 852.3	-7.3 ± 111.6	0.922 ± 0.005	0.907 ± 0.006	0.830 ± 0.005	HPF_1
2459058.8913	264.0 ± 131.8	13.0 ± 746.9	-54.5 ± 166.6	0.880 ± 0.005	0.828 ± 0.007	0.769 ± 0.006	HPF_1
2459058.8953	99.3 ± 155.0	111.0 ± 605.8	-126.8 ± 187.4	0.917 ± 0.004	0.864 ± 0.005	0.810 ± 0.004	HPF_1
2459058.8993	61.5 ± 118.1	-635.0 ± 465.8	202.7 ± 126.3	0.881 ± 0.003	0.839 ± 0.005	0.788 ± 0.004	HPF_1
2459104.9842	-330.7 ± 110.9	3389.0 ± 785.5	65.4 ± 142.2	0.906 ± 0.003	0.872 ± 0.004	0.804 ± 0.003	HPF_1
2459104.9881	-294.5 ± 137.2	1217.0 ± 519.8	-79.1 ± 179.2	0.950 ± 0.005	0.908 ± 0.007	0.853 ± 0.006	HPF_1
2459104.9921	-177.1 ± 114.1	1614.4 ± 1058.4	214.8 ± 121.7	0.914 ± 0.006	0.859 ± 0.008	0.802 ± 0.007	HPF_1
2459400.9444	-50.7 ± 137.3	46.5 ± 1697.5	-62.3 ± 175.9	0.885 ± 0.004	0.842 ± 0.005	0.787 ± 0.004	HPF_1
2459400.9485	-323.7 ± 78.7	511.6 ± 740.8	-24.9 ± 101.4	0.990 ± 0.005	0.946 ± 0.006	0.874 ± 0.005	HPF_1
2459400.9524	-85.6 ± 114.8	-324.9 ± 1476.3	6.0 ± 148.7	0.887 ± 0.004	0.836 ± 0.005	0.780 ± 0.004	HPF_1
2459401.9486	82.8 ± 106.2	-894.4 ± 1227.1	52.9 ± 134.6	0.885 ± 0.005	0.853 ± 0.006	0.782 ± 0.005	HPF_1
2459401.9524	82.6 ± 105.9	-57.7 ± 828.7	-102.3 ± 128.9	0.894 ± 0.006	0.854 ± 0.009	0.785 ± 0.007	HPF_1
2459401.9564	117.5 ± 62.4	-671.6 ± 877.2	-92.9 ± 69.8	0.913 ± 0.004	0.861 ± 0.005	0.800 ± 0.004	HPF ₁
2459411.9133	-231.0 ± 136.8	-895.4 ± 807.7	-119.4 ± 173.4	0.914 ± 0.004	0.891 ± 0.006	0.820 ± 0.005	HPF_1
2459411.9173	-244.0 ± 80.8	-185.5 ± 1436.3	98.3 ± 97.0	0.901 ± 0.004	0.867 ± 0.005	0.796 ± 0.004	HPF ₁
2459411.9213	-237.8 ± 156.4	55.1 ± 1373.5	80.8 ± 201.3	0.912 ± 0.004	0.890 ± 0.005	0.813 ± 0.004	HPF_1
2459423.8914	-347.1 ± 244.4	4045.9 ± 1976.9	628.5 ± 191.1	0.896 ± 0.003	0.853 ± 0.004	0.784 ± 0.003	HPF_1
2459423.8953	-391.1 ± 137.3	2182.3 ± 1391.2	-172.4 ± 166.6	0.926 ± 0.004	0.882 ± 0.006	0.821 ± 0.005	HPF ₁
2459423.8993	-274.3 ± 113.3	1276.9 ± 1382.9	49.0 ± 147.7	0.917 ± 0.004	0.870 ± 0.005	0.811 ± 0.004	HPF ₁
2459426.8845	-83.0 ± 96.8	-1617.2 ± 1388.4	148.2 ± 109.4	0.885 ± 0.003	0.863 ± 0.005	0.785 ± 0.004	HPF ₁
2459426.8884	-78.5 ± 128.4	-558.8 ± 841.1	-29.7 ± 162.7	0.898 ± 0.006	0.833 ± 0.008	0.792 ± 0.006	HPF ₁
2459426.8922	322.0 ± 107.1	764.7 ± 942.5	187.1 ± 116.6	0.896 ± 0.004	0.868 ± 0.005	0.801 ± 0.004	HPF_1

Table A1 (Continued)

BJD _{TDB} (day)	RV (m s ⁻¹)	dLW (m2 s-2)	$\begin{array}{c} CRX \\ (m \ s^{-1} \ Np^{-1}) \end{array}$	Ca II IRT 1	Ca II IRT 2	Ca II IRT 3	Instrument
2459806.8532	-97.8 ± 189.9	-1311.9 ± 1378.7	234.4 ± 227.1	0.866 ± 0.006	0.839 ± 0.009	0.809 ± 0.007	HPF ₂
2459806.8572	-87.3 ± 188.2	-578.3 ± 933.8	57.0 ± 242.8	0.879 ± 0.005	0.839 ± 0.007	0.805 ± 0.006	HPF_2
2459806.8612	-6.1 ± 207.1	2178.7 ± 1154.6	-17.9 ± 264.0	0.894 ± 0.005	0.853 ± 0.007	0.814 ± 0.006	HPF_2
2459827.7790	166.7 ± 198.2	3433.1 ± 1527.6	-15.7 ± 253.7	0.902 ± 0.004	0.862 ± 0.006	0.826 ± 0.005	HPF_2
2459827.7831	187.1 ± 213.5	1850.9 ± 1244.2	150.3 ± 266.7	0.873 ± 0.004	0.831 ± 0.005	0.792 ± 0.004	HPF_2
2459827.7870	-29.1 ± 215.6	2862.2 ± 472.5	277.7 ± 250.5	0.872 ± 0.003	0.824 ± 0.004	0.798 ± 0.004	HPF_2
2459828.7889	200.4 ± 134.9	734.7 ± 822.9	-214.9 ± 148.3	0.975 ± 0.005	0.934 ± 0.006	0.897 ± 0.005	HPF_2
2459828.7930	250.6 ± 96.1	-945.7 ± 1387.6	80.4 ± 117.3	0.891 ± 0.004	0.852 ± 0.005	0.812 ± 0.004	HPF_2
2459828.7969	473.0 ± 88.8	-1934.0 ± 985.7	187.4 ± 84.1	0.980 ± 0.004	0.943 ± 0.006	0.893 ± 0.005	HPF_2
2459843.9687	108.7 ± 145.1	153.8 ± 1164.0	137.5 ± 179.4	0.979 ± 0.005	0.953 ± 0.006	0.901 ± 0.005	HPF_2
2459843.9726	503.7 ± 104.7	-648.3 ± 930.0	15.3 ± 133.8	0.878 ± 0.004	0.845 ± 0.006	0.799 ± 0.005	HPF_2
2459843.9766	443.3 ± 120.7	-66.9 ± 1021.6	-177.8 ± 137.5	0.901 ± 0.004	0.860 ± 0.006	0.818 ± 0.005	HPF_2
2459886.6248	-338.5 ± 173.9	986.6 ± 1477.8	4.2 ± 222.7	0.899 ± 0.005	0.870 ± 0.007	0.811 ± 0.006	HPF_2
2459886.6287	-367.5 ± 147.8	85.6 ± 1266.4	125.4 ± 179.0	0.888 ± 0.003	0.846 ± 0.005	0.810 ± 0.004	HPF_2
2459886.6327	-385.8 ± 92.5	-794.3 ± 967.1	-10.9 ± 115.9	0.886 ± 0.004	0.833 ± 0.005	0.797 ± 0.004	HPF_2
2459890.6280	-252.9 ± 84.2	-397.4 ± 780.5	-130.9 ± 91.9	0.881 ± 0.004	0.852 ± 0.006	0.802 ± 0.005	HPF_2
2459890.6320	-250.1 ± 84.7	-431.2 ± 843.3	-107.1 ± 97.4	0.859 ± 0.003	0.813 ± 0.005	0.784 ± 0.004	HPF_2
2459890.6360	-252.1 ± 122.3	-1085.1 ± 1131.8	-139.2 ± 142.8	0.893 ± 0.005	0.863 ± 0.007	0.836 ± 0.006	HPF_2
2459913.5496	64.0 ± 119.9	-2167.1 ± 1539.5	-47.9 ± 153.7	0.902 ± 0.004	0.859 ± 0.005	0.813 ± 0.004	HPF_2
2459913.5538	52.4 ± 245.7	-432.6 ± 1550.5	85.9 ± 312.8	0.894 ± 0.004	0.840 ± 0.005	0.811 ± 0.004	HPF_2
2459913.5577	34.5 ± 178.7	-1463.2 ± 2104.6	-283.8 ± 198.2	0.902 ± 0.004	0.850 ± 0.006	0.825 ± 0.005	HPF_2

(This table is available in machine-readable form.)

Appendix B Results of Models 1 and 2 Fit

Tables B1 and B2 summarize the prior choices and results of the Model 1 and 2 fits, respectively. Figures B1 and B2 display the best-fit phased RV curve and posterior distributions of the planetary parameters of Models 1 and 2, respectively. See Sections 4.5.1 and 4.5.2 for details.

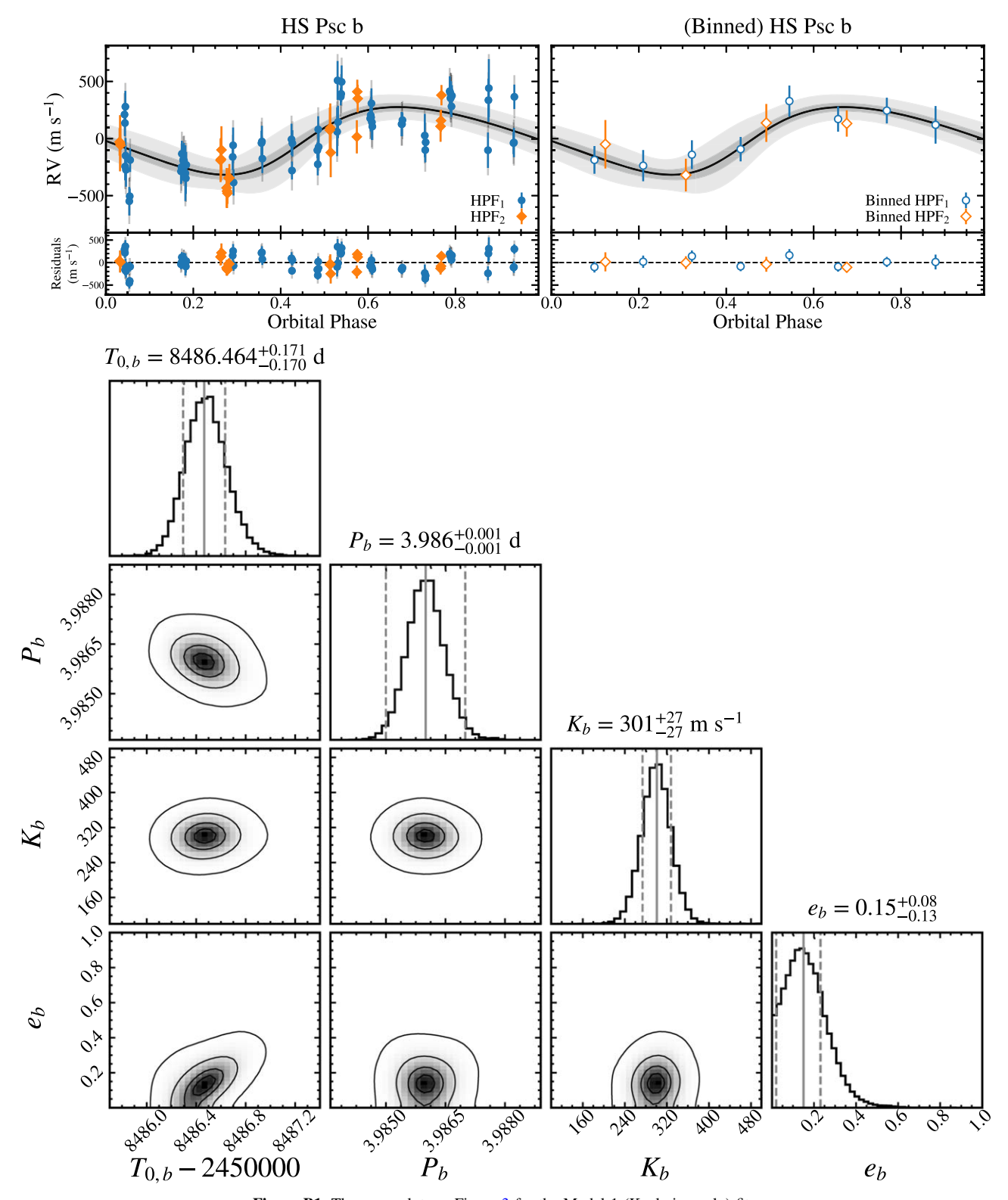
 Table B1

 Parameter Priors and Posteriors from the Keplerian-only Fit (Model 1) to the HPF Radial Velocities of HS Psc

Parameter	Prior	MAP	Median $\pm~1\sigma$	
	Fitted Param	eters		
	Keplerian and Instrume	ntal Parameters		
P_b (day)	U[0.5, 10.0]	3.986	$3.986^{+0.001}_{-0.001}$	
$T_{0,b}$ (day)	$\mathcal{U}[2458483.0, 2458487.5]$	2458486.494	$2458486.464_{-0.170}^{+0.171}$	
$K_b \text{ (m s}^{-1}\text{)}$	U[1.0, 1000.0]	296.5	301 ± 27	
$\sqrt{e_b} \sin \omega_*$	$\mathcal{U}[-1,1]$	-0.39	$-0.20^{+0.22}_{-0.24}$	
$\sqrt{e_b}\cos\omega_*$	$\mathcal{U}[-1,1]$	-0.17	$-0.22^{+0.18}_{-0.22}$	
$\sigma_{\text{HPF}_1} \text{ (m s}^{-1})$	$\mathcal{J}(1, 100)$	155.9	$161.3^{+21.0}_{-24.6}$	
$\sigma_{\text{HPF}_2} \text{ (m s}^{-1})$	$\mathcal{J}(1, 100)$	0.0	$17.4_{-17.4}^{+27.2} \\ -0.037_{-0.026}^{+0.025}$	
$\gamma_{\rm HPF_1} \ ({\rm km\ s}^{-1})$	$\mathcal{U}[-1.0922, 0.9655]$	-0.043		
$\gamma_{\mathrm{HPF}_2} \; (\mathrm{km} \; \mathrm{s}^{-1})$	U[-0.8858, 1.0037]	0.093	$0.083^{+0.037}_{-0.035}$	
	Derived Parar	neters		
$m_b \sin i \ (M_{\text{Jup}})$		1.76	$1.78^{+0.22}_{-0.21}$	
a_b (au)		0.043	$0.043^{+0.002}_{-0.002}$	
$T_{\text{peri,b}}$ (day)	•••	2458488.13	$2458487.56_{-0.41}^{+0.79}$	
e_b		0.18	$0.15^{+0.08}_{-0.13}$	
ω_* (°)		247.19	$218.98^{+58.57}_{-37.05}$	

Table B2
Parameter Priors and Posteriors from the Keplerian and Quasiperiodic Gaussian Process Fit (Model 2) to the HPF Radial Velocities of HS Psc

Parameter	Prior	MAP	Median \pm 1σ	
	Fitted Param	eters		
	Keplerian and Instrume	ntal Parameters		
P_b (d)	U[3.5, 4.5]	3.987	$3.986^{+0.005}_{-0.024}$	
$T_{0,b}$ (d)	$\mathcal{U}[2458485.0, 2458488.0]$	2458486.333	$2458486.422^{+0.409}_{-0.512}$	
$K_b \text{ (m s}^{-1})$	U[1.0, 1000.0]	273.9	264^{+84}_{-86}	
$\sqrt{e_b} \sin \omega_*$	$\mathcal{U}[-1,1]$	0.09	$0.04^{+0.43}_{-0.48}$	
$\sqrt{e_b}\cos\omega_*$	$\mathcal{U}[-1,1]$	-0.23	$-0.11^{+0.38}_{-0.37}$	
$\sigma_{\text{HPF}_1} \text{ (m s}^{-1})$	$\mathcal{J}(1, 100)$	0.1	$8.0^{+10.7}_{-8.0}$	
$\sigma_{HPF_2} \text{ (m s}^{-1}\text{)}$	$\mathcal{J}(1, 100)$	0.1	$8.1^{+11.7}_{-8.1}$	
$\gamma_{\mathrm{HPF_1}} \ (\mathrm{km \ s^{-1}})$	U[-1.0922, 0.9655]	-0.031	$-0.040^{+0.050}_{-0.052}$	
$\gamma_{\rm HPF_2} \ ({\rm km\ s^{-1}})$	$\mathcal{U}[-0.8858, 1.0037]$	0.050	$0.065^{+0.094}_{-0.089}$	
	QP Kernel Hyperp	parameters		
$A \text{ (m s}^{-1})$	$\mathcal{U}[0.0,1000.0]$	141.2	$185.2^{+40.1}_{-54.6}$	
λ_e	U[0.01, 5.0]	3.82	$2.07^{+1.07}_{-2.06}$	
λ_p	U[0.01, 5.0]	0.25	$0.30^{+0.14}_{-0.27}$	
P_{GP}	$\mathcal{N}[1.09,0.02]$	1.08	$1.09^{+0.02}_{-0.02}$	
	Derived Parar	neters		
$m_b \sin i \ (M_{\text{Jup}})$		1.78	$1.46^{+0.54}_{-0.43}$	
a_b (au)		0.044	$0.044^{+0.002}_{-0.002}$	
$T_{\text{peri, b}}$ (d)		2458487.03	$2458486.78^{+1.35}_{-0.93}$	
e_b		0.06	$0.25^{+0.19}_{-0.25}$	
ω_* (°)		159.55	$170.36^{+99.69}_{-100.95}$	



 $\textbf{Figure B1.} \ \text{The same plots as Figure 3 for the Model 1 (Keplerian-only) fits.}$

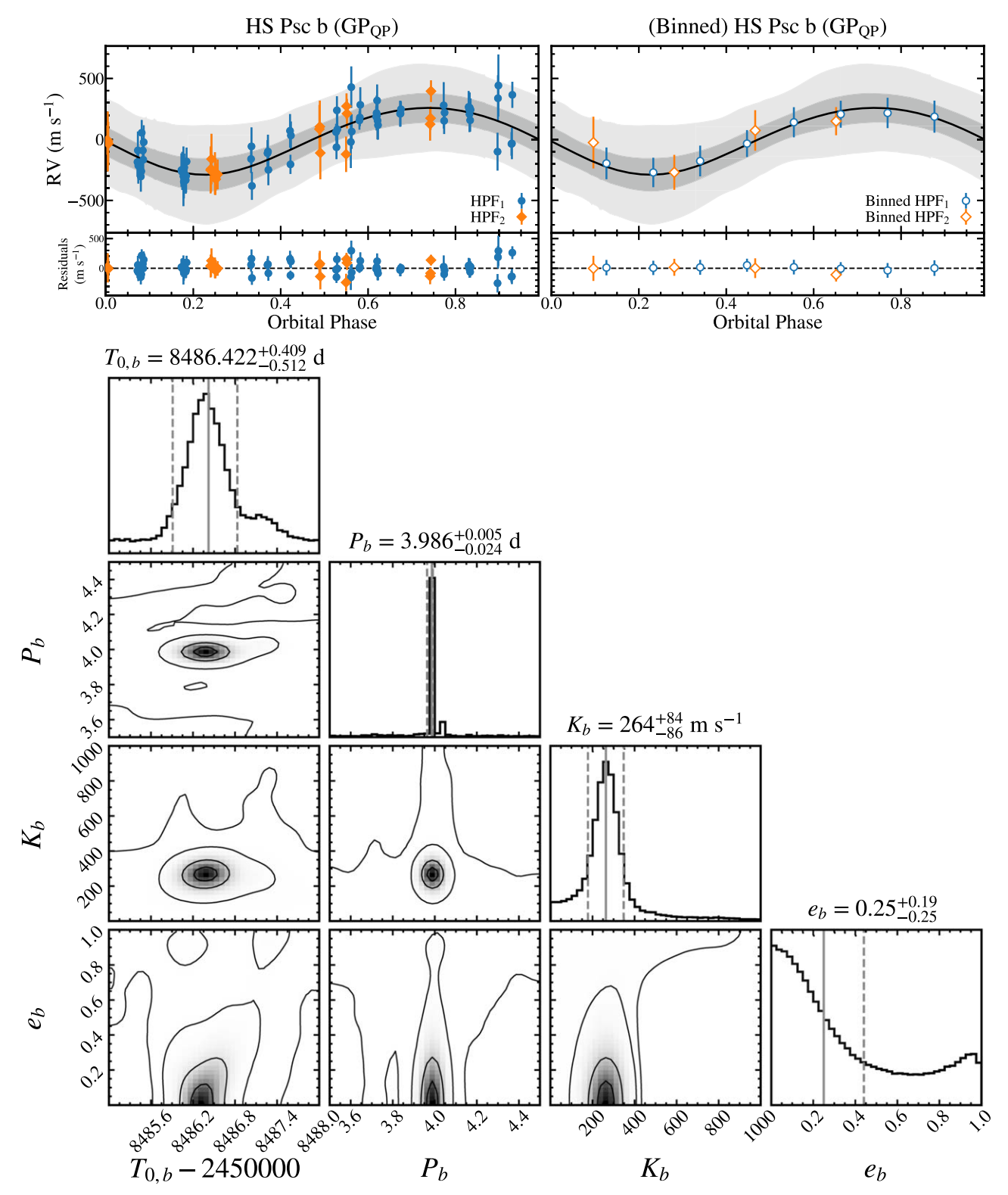


Figure B2. The same plots as Figure 3 for the Model 2 (Keplerian and QP GP) fits.

9596-7983

ORCID iDs

```
Quang H. Tran https://orcid.org/0000-0001-6532-6755
Brendan P. Bowler https://orcid.org/0000-0003-2649-2288
William D. Cochran https://orcid.org/0000-0001-9662-3496
Samuel Halverson https://orcid.org/0000-0003-1312-9391
Suvrath Mahadevan https://orcid.org/0000-0001-
```

Joe P. Ninan https://orcid.org/0000-0001-8720-5612
Paul Robertson https://orcid.org/0000-0003-0149-9678
Guðmundur Stefánsson https://orcid.org/0000-0001-7409-5688

Ryan C. Terrien https://orcid.org/0000-0002-4788-8858

References

```
Adams, F. C., & Laughlin, G. 2006, ApJ, 649, 1004
Affer, L., Micela, G., Damasso, M., et al. 2016, A&A, 593, A117
Aigrain, S., & Foreman-Mackey, D. 2023, ARA&A, 61, 329
Aigrain, S., Pont, F., & Zucker, S. 2012, MNRAS, 419, 3147
Akaike, H. 1981, J. Econom., 16, 3
Akaike, H. 1998, in Information Theory and an Extension of the Maximum
   Likelihood Principle, ed. E. Parzen, K. Tanabe, & G. Kitagawa (New York:
   Springer), 199
Albrecht, S. H., Dawson, R. I., & Winn, J. N. 2022, PASP, 134, 082001
Allard, F., Homeier, D., & Freytag, B. 2011, in ASP Conf. Ser. 448, 16th
   Cambridge Workshop on Cool Stars, Stellar Systems, and the Sun, ed.
   C. Johns-Krull, M. K. Browning, & A. A West (San Francisco, CA:
Angus, R., Morton, T., Aigrain, S., Foreman-Mackey, D., & Rajpaul, V. 2018,
    MNRAS, 474, 2094
Astropy Collaboration, Price-Whelan, A. M., Lim, P. L., et al. 2022, ApJ,
   935, 167
Astropy Collaboration, Price-Whelan, A. M., Sipőcz, B. M., et al. 2018, AJ,
   156, 123
Astropy Collaboration, Robitaille, T. P., Tollerud, E. J., et al. 2013, A&A,
  558, A33
Bailey, J. I., White, R. J., Blake, C. H., et al. 2012, ApJ, 749, 16
Baraffe, I., Chabrier, G., Barman, T. S., Allard, F., & Hauschildt, P. H. 2003,
    &A, 402, 701
Barenfeld, S. A., Bubar, E. J., Mamajek, E. E., & Young, P. A. 2013, ApJ,
Barragán, O., Aigrain, S., Rajpaul, V. M., & Zicher, N. 2022, MNRAS,
  509, 866
Barragán, O., Gandolfi, D., & Antoniciello, G. 2019, MNRAS, 482, 1017
Batygin, K., Bodenheimer, P. H., & Laughlin, G. P. 2016, ApJ, 829, 114
Benatti, S., Damasso, M., Borsa, F., et al. 2021, A&A, 650, A66
Blunt, S., Carvalho, A., David, T. J., et al. 2023, AJ, 166, 62
Boisse, I., Bouchy, F., Hébrard, G., et al. 2011, A&A, 528, A4
Boley, A. C., Granados Contreras, A. P., & Gladman, B. 2016, ApJL, 817, L17
Bouma, L. G., Hartman, J. D., Brahm, R., et al. 2020a, AJ, 160, 239
Bouma, L. G., Winn, J. N., Ricker, G. R., et al. 2020b, AJ, 160, 86
Bowler, B. P., Hinkley, S., Ziegler, C., et al. 2019, ApJ, 877, 60
Bowler, B. P., Liu, M. C., Shkolnik, E. L., & Tamura, M. 2015, ApJS, 216, 7
Bowler, B. P., Tran, Q. H., Zhang, Z., et al. 2023, AJ, 165, 164
Brandt, T. D., Kuzuhara, M., McElwain, M. W., et al. 2014, ApJ, 786, 1
Buchner, J., Georgakakis, A., Nandra, K., et al. 2014, A&A, 564, A125
Burnham, K. P., & Anderson, D. R. 2004, Sociological Methods & Research,
Burrows, A., Hubbard, W. B., Lunine, J. I., & Liebert, J. 2001, RvMP, 73, 719
Carleo, I., Benatti, S., Lanza, A. F., et al. 2018, A&A, 613, A50
Carleo, I., Malavolta, L., Lanza, A. F., et al. 2020, A&A, 638, A5
Carmona, A., Delfosse, X., Bellotti, S., et al. 2023, A&A, 674, A110
Castelli, F., & Kurucz, R. L. 2003, in IAU Symp. 210, Modelling of Stellar
   Atmospheres, ed. N. Piskunov, W. W. Weiss, & D. F. Gray (San Francisco,
   CA: ASP), A20
Chabrier, G. 2003, PASP, 115, 763
Choi, J., Dotter, A., Conroy, C., et al. 2016, ApJ, 823, 102
Cloutier, R., Astudillo-Defru, N., Doyon, R., et al. 2017, A&A, 608, A35
Crockett, C. J., Mahmud, N. I., Prato, L., et al. 2012, ApJ, 761, 164
Csizmadia, S., Hatzes, A., Gandolfi, D., et al. 2015, A&A, 584, A13
Cutri, R. M., Skrutskie, M. F., van Dyk, S., et al. 2003, yCat, II/246
```

```
Cutri, R. M., Wright, E. L., Conrow, T., et al. 2021, yCat, II/328
Dai, F., Winn, J. N., Gandolfi, D., et al. 2017, AJ, 154, 226
Damasso, M., & Del Sordo, F. 2017, A&A, 599, A126
David, T. J., Hillenbrand, L. A., Petigura, E. A., et al. 2016, Natur,
  534, 658
Dawson, R. I., & Johnson, J. A. 2018, ARA&A, 56, 175
Donati, J. F., Moutou, C., Malo, L., et al. 2016, Natur, 534, 662
Dotter, A. 2016, ApJS, 222, 8
Fabrycky, D., & Tremaine, S. 2007, ApJ, 669, 1298
Faria, J. P., Adibekyan, V., Amazo-Gómez, E. M., et al. 2020, A&A, 635, A13
Faria, J. P., Haywood, R. D., Brewer, B. J., et al. 2016, A&A, 588, A31
Feroz, F., Hobson, M. P., & Bridges, M. 2009, MNRAS, 398, 1601
Feroz, F., Hobson, M. P., Cameron, E., & Pettitt, A. N. 2019, OJAp, 2, 10
Ferraz-Mello, S., Rodríguez, A., & Hussmann, H. 2008, CeMDA, 101, 171
Figueira, P., Marmier, M., Bonfils, X., et al. 2010, A&A, 513, L8
Foreman-Mackey, D. 2018, RNAAS, 2, 31
Foreman-Mackey, D., Agol, E., Ambikasaran, S., & Angus, R. 2017, AJ,
Foreman-Mackey, D., Farr, W., Sinha, M., et al. 2019, JOSS, 4, 1864
Foreman-Mackey, D., Hogg, D. W., Lang, D., & Goodman, J. 2013, PASP,
Fortney, J. J., Marley, M. S., & Barnes, J. W. 2007, ApJ, 659, 1661
Gagné, J., Fontaine, G., Simon, A., & Faherty, J. K. 2018a, ApJL, 861, L13
Gagné, J., Mamajek, E. E., Malo, L., et al. 2018b, ApJ, 856, 23
Gagné, J., Plavchan, P., Gao, P., et al. 2016, ApJ, 822, 40
Gaia Collaboration, Brown, A. G. A., Vallenari, A., et al. 2018, A&A, 616, A1
Gaia Collaboration, Brown, A. G. A., Vallenari, A., et al. 2021, A&A, 649, A1
Gaia Collaboration, Vallenari, A., Brown, A. G. A., et al. 2022, arXiv:2208.
  00211
Gelfand, A., Dey, D., & Chang, H. 1992, Model Determination Using
  Predictive Distributions with Implementation Via Sampling-based Methods
  (Stanford, CA: Stanford Univ. Dept of Statistics)
Gelman, A., & Rubin, D. B. 1992, StaSc, 7, 457
Gilbertson, C., Ford, E. B., Jones, D. E., & Stenning, D. C. 2020, ApJ,
  905, 155
Ginsburg, A., Sipőcz, B. M., Brasseur, C. E., et al. 2019, AJ, 157, 98
Goldreich, P., & Soter, S. 1966, Icar, 5, 375
Goldreich, P., & Tremaine, S. 1980, ApJ, 241, 425
Gray, D. F. 1992, The Observation and Analysis of Stellar Photospheres,
   Vol.20 (Cambridge: Cambridge Univ. Press)
Green, G. 2018, JOSS, 3, 695
Greene, T. P., Tokunaga, A. T., Toomey, D. W., & Carr, J. B. 1993, Proc.
   SPIE, 1946, 313
Gregory, P. C. 2005, ApJ, 631, 1198
Grether, D., & Lineweaver, C. H. 2006, ApJ, 640, 1051
Grunblatt, S. K., Howard, A. W., & Haywood, R. D. 2015, ApJ, 808, 127
Gupta, A., & Schlichting, H. E. 2019, MNRAS, 487, 24
Gupta, A., & Schlichting, H. E. 2020, MNRAS, 493, 792
Haywood, R. D., Collier Cameron, A., Queloz, D., et al. 2014, MNRAS,
  443, 2517
Hernán-Obispo, M., Gálvez-Ortiz, M. C., Anglada-Escudé, G., et al. 2010,
   A&A, 512, A45
Hernán-Obispo, M., Tuomi, M., Gálvez-Ortiz, M. C., et al. 2015, A&A,
  576, A66
Higson, E., Handley, W., Hobson, M., & Lasenby, A. 2019, Statistics and
     omputing, 29, 891
Hill, G. J., Lee, H., MacQueen, P. J., et al. 2021, AJ, 162, 298
Hunter, J. D. 2007, CSE, 9, 90
Husser, T. O., Wende-von Berg, S., Dreizler, S., et al. 2013, A&A, 553, A6
Jackson, B., Greenberg, R., & Barnes, R. 2008, ApJ, 678, 1396
Jenkins, J. M., Twicken, J. D., McCauliff, S., et al. 2016, Proc. SPIE, 9913,
  99133E
Johns-Krull, C. M., McLane, J. N., Prato, L., et al. 2016, ApJ, 826, 206
Johnson, J. A., Aller, K. M., Howard, A. W., & Crepp, J. R. 2010, PASP,
   122, 905
Kanodia, S., Mahadevan, S., Ramsey, L. W., et al. 2018, Proc. SPIE, 10702,
Kanodia, S., & Wright, J. 2018, RNAAS, 2, 4
Kaplan, K. F., Bender, C. F., Terrien, R. C., et al. 2019, in ASP Conf. Ser. 523,
  Astronomical Data Analysis Software and Systems XXVII, ed. P. J. Teuben
  et al. (San Francisco, CA: ASP), 567
Kiefer, F., Hébrard, G., Sahlmann, J., et al. 2019, A&A, 631, A125
Kley, W., & Nelson, R. P. 2012, ARA&A, 50, 211
Koposov, S., Speagle, J., Barbary, K., et al. 2023, joshspeagle/dynesty: v2.1.0,
  Zenodo, doi:10.5281/zenodo.7600689
Kurucz, R. L. 1993, yCat, VI/39
```

Liddle, A. R. 2007, MNRAS, 377, L74

```
Lightkurve Collaboration, Cardoso, J. V. d. M., Hedges, C., et al., 2018
   Lightkurve: Kepler and TESS time series analysis in Python, Astrophysics
   Source Code Library, ascl:1812.013
Lindegren, L. 2018, http://rssd.esa.int/doc_fetch.php?id=3757412
Lopez, E. D., Fortney, J. J., & Miller, N. 2012, ApJ, 761, 59
Ma, B., & Ge, J. 2014, MNRAS, 439, 2781
Mahadevan, S., Ramsey, L., Bender, C., et al. 2012, Proc. SPIE, 8446, 84461S
Mahadevan, S., Ramsey, L. W., Terrien, R., et al. 2014, Proc. SPIE, 9147,
Mahmud, N. I., Crockett, C. J., Johns-Krull, C. M., et al. 2011, ApJ, 736, 123
Malo, L., Doyon, R., Lafrenière, D., et al. 2013, ApJ, 762, 88
Mann, A. W., Gaidos, E., Vanderburg, A., et al. 2017, AJ, 153, 64
Mann, A. W., Newton, E. R., Rizzuto, A. C., et al. 2016, AJ, 152, 61
MAST Team 2021, TESS Light Curves—All Sectors, STScI/MAST, doi:10.
   17909/T9-NMC8-F686
Masuda, K., & Winn, J. N. 2020, AJ, 159, 81
McCarthy, K., & White, R. J. 2012, AJ, 143, 134
McKinney, W. 2010, in Proc. of the 9th Python in Science Conf., ed.
   S. van der Walt & J. Millman (Austin, TX: SciPy), 56
Metcalf, A. J., Anderson, T., Bender, C. F., et al. 2019, Optic, 6, 233
Meunier, N., & Lagrange, A. M. 2013, A&A, 551, A101
Morley, C. V., Mukherjee, S., Marley, M. S., et al. 2024, arXiv:2402.00758
Morton, T. D., 2015 isochrones: Stellar model grid package, Astrophysics
  Source Code Library, ascl:1503.010
Naoz, S., Farr, W. M., Lithwick, Y., Rasio, F. A., & Teyssandier, J. 2011,
   Natur, 473, 187
Newton, E. R., Mann, A. W., Tofflemire, B. M., et al. 2019, ApJL, 880, L17
Ninan, J. P., Bender, C. F., Mahadevan, S., et al. 2018, Proc. SPIE, 10709,
Ninan, J. P., Mahadevan, S., Stefansson, G., et al. 2019, JATIS, 5, 041511
Norton, A. J., Wheatley, P. J., West, R. G., et al. 2007, A&A, 467, 785
Oelkers, R. J., Rodriguez, J. E., Stassun, K. G., et al. 2018, AJ, 155, 39
Owen, J. E., & Wu, Y. 2013, ApJ, 775, 105
Prato, L., Huerta, M., Johns-Krull, C. M., et al. 2008, ApJL, 687, L103
Queloz, D., Henry, G. W., Sivan, J. P., et al. 2001, A&A, 379, 279
Raftery, A. E. 1986, Am. Sociol. Rev., 51, 145
Ramsey, L. W., Adams, M. T., Barnes, T. G., et al. 1998, Proc. SPIE, 3352, 34
Ranc, C., Cassan, A., Albrow, M. D., et al. 2015, A&A, 580, A125
Ricker, G. R., Winn, J. N., Vanderspek, R., et al. 2015, JATIS, 1, 014003
Rizzuto, A. C., Mann, A. W., Vanderburg, A., Kraus, A. L., & Covey, K. R.
   2017, AJ, 154, 224
Rizzuto, A. C., Newton, E. R., Mann, A. W., et al. 2020, AJ, 160, 33
Rizzuto, A. C., Vanderburg, A., Mann, A. W., et al. 2018, AJ, 156, 195
Sahlmann, J., Ségransan, D., Queloz, D., et al. 2011, A&A, 525, A95
Santerne, A., Moutou, C., Tsantaki, M., et al. 2016, A&A, 587, A64
```

Savitzky, A., & Golay, M. J. E. 1964, AnaCh, 36, 1627

```
Schlafly, E. F., & Finkbeiner, D. P. 2011, ApJ, 737, 103
Schlegel, D. J., Finkbeiner, D. P., & Davis, M. 1998, ApJ, 500, 525
Schlieder, J. E., Lépine, S., & Simon, M. 2010, AJ, 140, 119
Schwarz, G. 1978, AnSta, 6, 461
Sharma, S. 2017, ARA&A, 55, 213
Shetrone, M., Cornell, M. E., Fowler, J. R., et al. 2007, PASP, 119, 556
Skilling, J. 2004, in AIP Conf. Ser. 735, Bayesian Inference and Maximum
   Entropy Methods in Science and Engineering, ed. R. Fischer, R. Preuss, &
   U. V. Toussaint (Melville, NY: AIP), 395
Skilling, J. 2006, BayAn, 1, 833
Smith, J. C., Stumpe, M. C., Van Cleve, J. E., et al. 2012, PASP, 124, 1000
Speagle, J. S. 2020, MNRAS, 493, 3132
Stassun, K. G., Oelkers, R. J., Paegert, M., et al. 2019, AJ, 158, 138
Stassun, K. G., & Torres, G. 2021, ApJL, 907, L33
Stefansson, G., Cañas, C., Wisniewski, J., et al. 2020a, AJ, 159, 100
Stefansson, G., Hearty, F., Robertson, P., et al. 2016, ApJ, 833, 175
Stefansson, G., Mahadevan, S., Maney, M., et al. 2020b, AJ, 160, 192
Stefansson, G., Mahadevan, S., Petrovich, C., et al. 2022, ApJL, 931, L15
Stumpe, M. C., Smith, J. C., Catanzarite, J. H., et al. 2014, PASP, 126, 100
Stumpe, M. C., Smith, J. C., Van Cleve, J. E., et al. 2012, PASP, 124, 985
Suzuki, R., Kudo, T., Hashimoto, J., et al. 2010, Proc. SPIE, 7735, 773530
Tayar, J., Claytor, Z. R., Huber, D., & van Saders, J. 2022, ApJ, 927, 31
Torres, G., Andersen, J., & Giménez, A. 2010, A&ARv, 18, 67
Tran, Q. H., Bedell, M., Foreman-Mackey, D., & Luger, R. 2023, ApJ,
  950, 162,
Tran, Q. H., Bowler, B. P., Cochran, W. D., et al. 2021, AJ, 161, 173
Tran, Q. H., Bowler, B. P., Endl, M., et al. 2022, AJ, 163, 225
Triaud, A. H. M. J., Collier Cameron, A., Queloz, D., et al. 2010, A&A,
Tuomi, M., Jones, H. R. A., Barnes, J. R., et al. 2018, AJ, 155, 192
van der Walt, S., Colbert, S. C., & Varoquaux, G. 2011, CSE, 13, 22
van Eyken, J. C., Ciardi, D. R., von Braun, K., et al. 2012, ApJ, 755, 42
Vines, J. I., & Jenkins, J. S. 2022, MNRAS, 513, 2719
Virtanen, P., Gommers, R., Oliphant, T. E., et al. 2020, NatMe, 17, 261
Ward, W. R. 1997, Icar, 126, 261
Winn, J. N., Fabrycky, D., Albrecht, S., & Johnson, J. A. 2010, ApJL,
  718, L145
Wright, J. T., Marcy, G. W., Howard, A. W., et al. 2012, ApJ, 753, 160
Wright, J. T., Roy, A., Mahadevan, S., et al. 2013, ApJ, 770, 119
Wu, Y., & Murray, N. 2003, ApJ, 589, 605
Yee, S. W., Petigura, E. A., & von Braun, K. 2017, ApJ, 836, 77
Yu, L., Donati, J. F., Hébrard, E. M., et al. 2017, MNRAS, 467, 1342
Zacharias, N., Finch, C. T., Girard, T. M., et al. 2012, VizieR Online Data
  Catalog, I/322A
Zacharias, N., Finch, C. T., Girard, T. M., et al. 2013, AJ, 145, 44
Zechmeister, M., Reiners, A., Amado, P. J., et al. 2018, A&A, 609, A12
```